



No increase is detected and modeled for the seasonal cycle amplitude of $\delta^{13}\text{C}$ of atmospheric carbon dioxide

Fortunat Joos^{1,2}, Sebastian Lienert^{1,2}, and Sönke Zaehle³

¹Climate and Environmental Physics, University of Bern, Bern Switzerland

²Oeschger Centre for Climate Change Research, University of Bern, Bern, Switzerland

³Max Planck Institute for Biogeochemistry, P.O. Box 600164, Hans-Knöll-Str. 10, 07745 Jena, Germany

Correspondence: Fortunat Joos (fortunat.joos@unibe.ch)

Abstract. Measurements of the seasonal cycle of $\delta^{13}\text{C}(\text{CO}_2)$ provide information on the global carbon cycle and the regulation of carbon and water fluxes by leaf stomatal openings on ecosystem and decadal scales. Land biosphere carbon exchange is the primary driver of $\delta^{13}\text{C}(\text{CO}_2)$ seasonality in the Northern Hemisphere. We use isotope-enabled simulations of the Bern3D-LPX Earth System Model of Intermediate Complexity and fossil fuel emission estimates with a model of atmospheric transport to simulate local atmospheric $\delta^{13}\text{C}(\text{CO}_2)$. Unlike the observed growth of the seasonal amplitude of CO_2 at northern sites, no significant temporal trend in the seasonal amplitude of $\delta^{13}\text{C}(\text{CO}_2)$ is detected at most sites, consistent with the insignificant model trends. Comparing the preindustrial and modern periods, the modeled small amplitude changes at northern sites are linked to the near-equal increase of background atmospheric CO_2 and the seasonal signal of the net atmosphere-land $\delta^{13}\text{C}$ flux in the northern extratropical region, with no long-term temporal changes in the isotopic fractionation by C3 plants. The good data-model agreement in the seasonal amplitude of $\delta^{13}\text{C}(\text{CO}_2)$ and its decadal trend provides implicit support for the regulation of stomatal conductance by C3 plants towards intrinsic water use efficiency to grow proportionally to atmospheric CO_2 over recent decades. Disequilibrium fluxes contribute little to the seasonal amplitude of the net land isotope flux north of 40°N but contribute near-equally to the isotopic flux associated with growing season net carbon uptake in tropical and Southern Hemisphere ecosystems, pointing to the importance of monitoring $\delta^{13}\text{C}(\text{CO}_2)$ over these ecosystems. We propose to apply seasonally-resolved $\delta^{13}\text{C}(\text{CO}_2)$ observations as a novel constraint for land biosphere models and underlying processes for improved projections of the anthropogenic carbon sink.

1 Introduction

The seasonal variations in the carbon exchange fluxes between the atmosphere and the surface cause a seasonal cycle in atmospheric CO_2 (C_a) (Keeling et al., 1996; Graven et al., 2013; Masarie et al., 2014) and its stable isotopic signature ($\delta^{13}\text{C}_a$) (Keeling, 1960; Keeling et al., 1984, 1989, 2005; GLOBALVIEW-CO2C13, 2009). Observations of the atmospheric seasonal



cycles in background tropospheric air provide large-scale information on the carbon fluxes between the atmosphere, ocean, and land (Heimann et al., 1989, 1998) and constraints for models used to project atmospheric CO₂ and global warming.

The additional information of $\delta^{13}\text{C}$ data in comparison to carbon data stems from differences in fractionation for different carbon fluxes. Carbon isotopic fractionation describes the preferential transfer of light ^{12}C compared to heavier ^{13}C . The degree of fractionation is different for the different physical, chemical, and biological processes (Mook, 1986) causing differences in the isotopic composition of carbon reservoirs and fluxes. The seasonal atmospheric $\delta^{13}\text{C}$ variations result from the combination of carbon and isotopic fluxes from fossil fuel burning, land use, and the exchange with the ocean, and land biosphere. Comparing results of carbon isotope-enabled models with observations of $\delta^{13}\text{C}_a$ is useful to assess whether the mix of carbon and isotopic sink and source fluxes is represented consistently in comparison with the observations. $\delta^{13}\text{C}_a$ observations offer, therefore, a benchmark for evaluating and improving earth system models.

Fractionation is particularly large during the assimilation of CO₂ from the atmosphere by plants following the C3 photosynthesis pathway which are responsible for most of the global productivity (Still et al., 2003). Importantly, changes in isotopic fractionation by C3 plants are indicative of changes in stomatal conductance, regulating the leaf-internal CO₂ mixing ratio, and thus photosynthesis (Farquhar, 1989; Saurer and Voelker, 2022; Cernusak and Ubierna, 2022). Photosynthesis, the associated water loss, and evaporative cooling are key characteristics of ecosystem function that are central to the cycles of carbon, nitrogen, water, and energy (Keenan et al., 2013; Knauer et al., 2017) and for the land sink of anthropogenic carbon. Acquisition of CO₂ for photosynthesis is accompanied by the loss of water through the stomatal pores that govern, by their conductance, the diffusion of these two gases between the leaf interior and the atmosphere. A key question is how ecosystems adjust their overall conductance and, thereby, co-regulate carbon uptake and plant growth, and water loss and evaporative cooling under rising atmospheric CO₂, growing nitrogen inputs to ecosystems, and increasing water vapor deficits under global warming. Many studies, relying on multi-decadal to century-scale tree-ring $\delta^{13}\text{C}$ records and free air CO₂ enrichment (FACE) experiments, suggest small changes in isotopic fractionation and intrinsic water use efficiency, the ratio of assimilation to conductance, to grow roughly proportionally with atmospheric CO₂ (Voelker et al., 2016; Saurer et al., 2014; Kauwe et al., 2013; Peñuelas et al., 2011; Keller et al., 2017; Frank et al., 2015). In contrast, Battipaglia et al. (2013) and Keenan et al. (2013) suggest a scenario where conductance and the flows of carbon and water are downregulated under increasing CO₂. Conflicting results for 20th-century changes in fractionation and intrinsic water use efficiency are also found in global land biosphere models (Keller et al., 2017). Upscaling of results from site studies to large scales is challenging. It remains to be assessed whether a scenario with small long-term changes in fractionation of C3 plants is compatible with atmospheric $\delta^{13}\text{C}_a$ observations representing carbon fluxes over large regions.

The observational records from globally distributed monitoring sites (Keeling et al., 1996; Graven et al., 2013; Masarie et al., 2014) demonstrate a significant growth trend in the seasonal cycle amplitude (*SA*) of C_a (Keeling et al., 1996; Graven et al., 2013). The observed seasonal cycle and amplitude growth of C_a are widely used to evaluate carbon cycle models and system understanding by transporting fluxes from terrestrial, oceanic, and fossil sources with a model of atmospheric transport to obtain local C_a anomalies (Heimann et al., 1998; Dargaville et al., 2002; Scholze et al., 2008; Peng et al., 2015; Lienert and Joos, 2018). Studies address the role of different climatic drivers and terrestrial carbon cycle processes such as drought,



land use, warming, productivity, and soil respiration (Heimann et al., 1989, 1998; Graven et al., 2013; Forkel et al., 2016; Ito et al., 2016; Bastos et al., 2019; Wang et al., 2020) and surface-to-atmosphere C fluxes (e.g. Peylin et al. (2013)). $SA(C_a)$ and their temporal trends at different monitoring sites are used for constraining an ensemble of land biosphere model simulations (Lienert and Joos, 2018).

Comparable studies, analyzing the temporal trends in $SA(\delta^{13}C_a)$ and the seasonal cycle of $\delta^{13}C_a$, are, to our knowledge, lacking. While seasonally-resolved atmospheric $\delta^{13}C_a$ measurements are available (GLOBALVIEW-CO2C13, 2009; Keeling et al., 2001), these seasonally-resolved records are yet to be fully utilized in the context of processed-based carbon cycle models. Heimann et al. (1989) simulated the spatiotemporal distribution of $\delta^{13}C_a$ and C_a with an atmospheric transport model using estimates of net primary productivity and heterotrophic respiration based on satellite data and surface temperature and prescribed surface ocean CO_2 , demonstrating the dominant role of land biosphere fluxes for northern hemisphere seasonality and finding relevant signals from the ocean and land in the southern hemisphere. Observations of $\delta^{13}C_a$ seasonal cycles have been used to investigate isotopic fractionation (Ballantyne et al., 2010) and trends in the phenology of northern terrestrial ecosystems (Gonsamo et al., 2017), but to our knowledge have not been used as a benchmark for model performance in combination with an atmospheric transport model and for analyzing trends in $SA(\delta^{13}C_a)$ globally.

This study addresses the following main questions:

1. Is the seasonal cycle of $\delta^{13}C_a$ observed at a network of globally distributed sites well represented in model simulations? How large are the contributions of ocean, land, and fossil fuel fluxes to $\delta^{13}C_a$ seasonality?
2. What are the temporal trends in $SA(\delta^{13}C_a)$ in the observational records and are the modeled trends in $SA(\delta^{13}C_a)$ consistent with the observed trends?
3. What are the different drivers of $SA(\delta^{13}C_a)$ versus $SA(C_a)$ and of their temporal trends? Is a model scenario with intrinsic water use efficiency growing proportional with atmospheric CO_2 consistent with $\delta^{13}C_a$ data?

We simulate atmospheric $\delta^{13}C_a$ and C_a at 19 sites using the matrix representation of an atmospheric transport model and net atmosphere-to-surface fluxes of CO_2 and $\delta^{13}(CO_2)$ from an Earth System Model of Intermediate Complexity (EMIC) alongside gridded fossil fuel emission estimates and changes in land use and the distribution of C3 and C4 crops. We compare model results to observations and analyze trends in $SA(\delta^{13}C_a)$ using the records of the Scripps CO_2 program (Keeling et al., 2001) and the Cooperative Global Atmospheric Data Integration Project (2013) product. We demonstrate for the first time that the observations at the globally distributed sites show no significant trends in the seasonal cycle amplitude of $\delta^{13}C_a$, consistent with our model chain, but surprising in view of the large trend in the seasonal amplitude of CO_2 . We discuss the implications of our results for changes in the fractionation by C3 plants, their stomatal controls, and associated carbon and water fluxes. We develop a theoretical framework to explain the trends in $SA(\delta^{13}C_a)$ and decompose net carbon and isotope land biosphere fluxes into underlying component fluxes and changes in carbon fluxes and fractionation. The framework could serve future studies, e.g., studies applying an ensemble of different models for multi-model evaluation and more robust conclusions in comparison to using a single model chain.



90 2 Methods

2.1 Bern3D-LPX

Spatially-resolved surface-to-atmosphere CO₂ and ¹³CO₂ fluxes are simulated with the EMIC Bern3D-LPX. Here, the ocean-atmosphere model Bern3D (Jeltsch-Thömmes and Joos, 2020; Battaglia and Joos, 2018; Ritz et al., 2011) is coupled to the Dynamic Global Vegetation Model (DGVM) LPX-Bern v1.4 (Lienert and Joos, 2018). The Bern3D model features a 41 x 40
95 horizontal ocean resolution (about 9°x4.5°) with 32 depth layers, coupled to a single-layer energy-moisture balance atmosphere (Ritz et al., 2011). In Bern3D, carbon and its isotopes are implemented as tracers with fractionation for air-sea and sea-air gas exchange, aquatic chemistry, and the production of organic material and CaCO₃ as a function of surface ocean temperature, aqueous CO₂, and the speciation of DIC as described by Jeltsch-Thömmes and Joos (2023). LPX-Bern simulates the coupled cycling of carbon, nitrogen, and water (Xu-Ri and Prentice, 2008; Wania et al., 2009a, b; Stocker et al., 2014) and vegetation
100 dynamics using plant functional types (Sitch et al., 2003). It is here run on a 3.75°x2.5° resolution. Grid cells are subdivided into different land use classes (mineral soil, wetlands, crop, pasture, urban). Carbon isotopes were added (Scholze et al., 2003) using a photosynthetic fractionation scheme (Lloyd and Farquhar, 1994) and without further isotopic fractionation during the transfer through vegetation, litter, soil, and product pools. The signature of respired carbon reflects the signature of carbon assimilated at previous times; the lag times between assimilation and respiration are dictated by the turnover time scales of
105 the various pools, depending on temperature and soil moisture. Land carbon and isotope fluxes respond to altered climate, which influences, for example, photosynthesis through temperature and water limitation, fire frequency, and autotrophic and heterotrophic respiration rates, to increasing CO₂, which stimulates photosynthesis and affects water use efficiency ("CO₂ fertilization"), and to land use (Strassmann et al., 2008), which causes, for example, transfer of tree carbon to the atmosphere, litter, and product pools after deforestation and shifts from natural vegetation to C3 and C4 crops and pasture, and to altered
110 nitrogen deposition and nitrogen fertilizer addition on managed land alleviating nitrogen limitation.

Bern3D and LPX-Bern were spun up individually, followed by a 500-year coupled spinup to pre-industrial equilibrium (1700 CE; 276.3 ppm, -6.27 ‰). A transient simulation, E_{standard}, from 1700 to 2020 is driven by annual fossil carbon emissions (including the contribution from cement production) (Friedlingstein et al., 2020), net land use area changes (Hurtt et al., 2020), and non-CO₂ radiative forcing. δ¹³C of the fossil fuel emissions follows Andres et al. (2017) for 1751-2014 and set to the
115 value for 1751 before. For 2014-2020, signatures of major source categories (coal, oil, gas, cement) are assumed constant and combined with the emission sources from Friedlingstein et al. (2020), following the approach of Andres et al. (2000). Here, we explicitly distinguish land use classes for C3 and C4 crops and prescribe their extent, and net land use area changes, based on LUH2 (Hurtt et al., 2020). Nitrogen deposition and nitrogen fertilization are taken from the NMIP project (Tian et al., 2018). Nitrogen (N) is a limiting nutrient in LPX and plant growth is downregulated under N-stress, which tends to reduce
120 plant growth and plant growth responses to rising CO₂ compared to a model with absent N cycling. The NCEP/NCAR monthly wind stress climatology (Kalnay et al., 1996) is prescribed to the ocean. Monthly climate fields from CRU-TS4.05 (Harris et al., 2020) are used for the land model. For 1700-1900 and the spinup, the climate of 1901-1931 is recycled. A control simulation (E_{control}) without anthropogenic CO₂ emissions, and absent radiative forcing from non-CO₂ agents (e.g., from CH₄, N₂O,



ozone), land use, nitrogen deposition, and nitrogen fertilization at 1700 level, as well as recycling 1901-1931 land climate
125 provides a baseline. Atmospheric CO₂ and δ¹³C evolve freely in all simulations presented and remain at their preindustrial
values in E_{control}.

2.2 Atmospheric Transport Model TM3 and the seasonal cycles of CO₂ and δ¹³C_a

We employ the transport matrices of the TM3 atmospheric transport model (Heimann and Körner, 2003; Kaminski et al., 1998;
Schürmann et al., 2016) to translate surface-atmosphere fluxes from Bern3D-LPX and fossil emissions into CO₂ (C_a) and
130 δ¹³C(CO₂) (δ¹³C_a) anomalies at 19 measurement sites across the globe. Before transport, the fluxes are remapped to the TM3
72x48 grid (5° × 3.75°). Here, the matrices span from 1982 to 2012 and are only available if there is also a CO₂ measurement
available at the corresponding site. Each matrix represents the sensitivity of the local atmospheric concentration for a given
month to the local surface fluxes of the previous period, spanning up to 48 months. The transport model is initialized with
equal C_a and δ¹³C_a at all sites.

135 For ¹³C, the signature-weighted net atmosphere-to-surface flux is:

$$\delta^{13}f_{as,net}(\mathbf{x},t) = f_{as,net}(\mathbf{x},t) \cdot \delta^{13}C_{as,net}(\mathbf{x},t). \quad (1)$$

δ¹³f_{as,net} is in units of mol permil m⁻² yr⁻¹. \mathbf{x} indicates location and t time at the monthly and spatial (5° × 3.75°) resolution
of TM3. The net carbon fluxes ($f_{as,net}$; mol m⁻² yr⁻¹), their signatures (δ¹³C_{as,net}), and, therefore, δ¹³f_{as,net}, are readily
available for fossil emissions, including cement production (Andres et al., 2009b, a). Bern3D-LPX simulates two-way exchange
140 of CO₂ and ¹³CO₂ from and to the ocean and land surface. Net transfer rates are determined by the difference of these gross
fluxes to yield atmosphere-to-surface net fluxes $f_{as,net}$ and δ¹³f_{as,net} of Bern3D-LPX.

The matrices are applied with $f_{as,net}$ to compute anomalies in C_a and with δ¹³f_{as,net} to compute anomalies in ¹³CO₂.
We get δ¹³C_a from ¹³CO₂/C_a. This method of transporting signature-weighted net fluxes was chosen instead of separately
transporting ¹³CO₂ and ¹²CO₂. Both approaches were tested and showed very similar results, except for numerical issues in
145 months having very small local ¹²CO₂ anomalies for the second approach.

Ocean, land, and fossil fluxes from the standard simulation are transported separately to quantify the contributions of these
individual components to the seasonal variations in C_a and δ¹³C_a. For E_{control}, fossil fuel fluxes are not transported, consistent
with the model setup.

2.3 Site data

150 Observations from 19 monitoring sites are used for comparison with simulated C_a and δ¹³C_a and to determine observation-
based trends in their SA. The Cooperative Global Atmospheric Data Integration Project (2013) product is used for C_a. For
δ¹³C_a, the records of the Scripps CO₂ program (Keeling et al., 2001) for Alert, Mauna Loa, and the South Pole from monthly-
averaged flask data are used. These records span a longer period than the available transport matrices. For the remaining 16
sites, the shorter (1994 to 2009) records of GLOBALVIEW-CO2C13 (2009) are used. In the main manuscript, we focus on 3 out



155 of the 19 available transport sites: Alert (82.5°N, Canada), Mauna Loa (19.5°N, Hawaii), and South Pole (90°S, Antarctica). Results for the other sites are shown in the supplementary and Table 1.

Additional $\delta^{13}\text{C}_a$ monthly flask data from the Scripps CO₂ program (Keeling et al., 2001) are used for analyzing temporal trends in the $SA(\delta^{13}\text{C}_a)$. We focus on eight sites with more than twenty years of data: Alert (ALT, 82°N), Point Barrow (PTB, 71°N, La Jolla (LJO, 33°N), Mauna Loa Observatory (MLO, 20°N), Cape Kumukahi (KUM, 20°N), Christmas Island (CHR, 160 2°N), Samoa (SAM, 14°S), and South Pole (SPO, 90°S). The records from Kermadec Island (KER, 29°S) and Baring Head, New Zealand (NZD, 41°S) extend over more than 20 years, but have often missing monthly values.

3 The influence of carbon and isotope fluxes on the seasonal cycles of CO₂ and $\delta^{13}\text{CO}_2$: a conceptual framework

We develop a simplified conceptual framework to qualitatively explore the influence of carbon and isotope fluxes on the seasonal cycles of C_a and $\delta^{13}\text{C}_a$. For illustration, the atmosphere is considered to be well mixed in this section; the atmospheric transport operator is linear and the findings may qualitatively also apply to spatially-resolved fluxes. The budgets for the 165 atmospheric inventories of carbon and ¹³C are approximated (Tans et al., 1993):

$$\frac{d}{dt}N_a = -F_{as,net} \quad (2)$$

$$\frac{d}{dt}(N_a \cdot \delta^{13}\text{C}_a) = \left(\frac{d}{dt}N_a\right) \cdot \delta^{13}\text{C}_a + N_a \cdot \left(\frac{d}{dt}\delta^{13}\text{C}_a\right) = -F_{as,net} \cdot \overline{\delta^{13}\text{C}_{as,net}} \quad (3)$$

170 N_a and $N_a \cdot \delta^{13}\text{C}_a$ are the atmospheric inventories of carbon and (approximately) of ¹³C (in mol permil). $F_{as,net}$ and $F_{as,net} \cdot \overline{\delta^{13}\text{C}_{as,net}}$ are the globally integrated net atmosphere-to-surface carbon and ¹³C flux; $\overline{\delta^{13}\text{C}_{as,net}}$ is the signature of the global net carbon flux. We set $N_a = c \cdot C_a$, where c is a unit conversion factor. Solving Eqs. 2 and 3 for the change in C_a and $\delta^{13}\text{C}_a$ yields:

$$\frac{d}{dt}C_a = \frac{-1}{c} \cdot F_{as,net} \quad (4)$$

175

$$\frac{d}{dt}\delta^{13}\text{C}_a = \frac{-1}{c \cdot C_a} \cdot \delta^{13}F_{as,net}^* \quad (5)$$

with $\delta^{13}F_{as,net}^*$ being the global integral of

$$\delta^{13}f_{as,net}^* = f_{as,net} \cdot (\delta^{13}\text{C}_{as,net} - \delta^{13}\text{C}_a) \quad (6)$$

The superscript * indicates that the ¹³C fluxes (e.g., in units of mol permil yr⁻¹ m⁻² for $\delta^{13}f_{as,net}^*$) are referenced to the atmospheric signature. Eq. 6 corresponds to Eq. 1 for the net atmosphere-to-surface isotopic flux but is now referenced to the atmospheric signature instead the signature of 0 permil of the Vienna Pee Dee Belemnite standard as in Eq. 1. In this way, a 180 positive (negative) flux causes a positive (negative) change in $\delta^{13}\text{C}_a$.



Eqs. 4 and 5 are readily integrated over the growing season from the intraannual maximum to the minimum (subscripts max, min) in C_a and the corresponding beginning, t_{beg} , and end time, t_{end} , of the growing season to get the seasonal cycle amplitude (SA) for the two tracers and (cumulative) net fluxes (see Appendix A for calculation of SA for a flux):

$$\underbrace{C_{a,max} - C_{a,min}}_{SA(C_a)} = \frac{1}{c} \underbrace{\int_{t_{beg}}^{t_{end}} dt F_{as,net}(t)}_{SA(F_{as,net})} \quad (7)$$

$$\underbrace{\delta^{13}C_{a,max} - \delta^{13}C_{a,min}}_{SA(\delta^{13}C_a)} = \frac{-1}{c \cdot C_a} \underbrace{\int_{t_{beg}}^{t_{end}} dt \delta^{13}F_{as,net}^*(t)}_{SA(\delta^{13}F_{as,net}^*)} \quad (8)$$

Eqs. 5 and 8 provide important insight. First, changes in $\delta^{13}C_a$ and its seasonal cycle are driven by $\delta^{13}F_{as,net}^*$; seasonal changes in C_a , the denominator in Eq. 5, are small compared to C_a and C_a considered constant within a given year (the error associated with this approximation is less than 3%). Second, the background CO_2 mixing ratio, C_a , modulates the magnitude of the $\delta^{13}C_a$ seasonal cycle. $SA(\delta^{13}C_a)$ would be larger under low preindustrial CO_2 than under modern CO_2 for equal seasonal variations in $\delta^{13}F_{as,net}^*$. Correspondingly, $SA(\delta^{13}C_a)$ does not change over time as long as relative changes in $SA(\delta^{13}F_{as,net}^*)$ and in CO_2 are equal. Equations 7 and 8 were derived for a globally well mixed atmosphere and global fluxes, but analogously also apply for the tracer seasonality at individual sites with the integral on the right-hand side of Eqs. 7 and 8 representing the integral of (transport-weighted) fluxes over the region influencing tracer seasonality at the site. We recall that the above equations and conclusions were derived by assuming a well-mixed atmosphere, while in reality spatial flux patterns and transport and their changes influence seasonal cycles at individual atmospheric sites. Further, the start and end of the growing season are assumed to coincide with the switch in the sign of the isotopic flux; this is the case in our model for zonally integrated fluxes. These seasonal fluxes will be presented in section 3.3. Equations 2 to 8 are for illustrating the influence of carbon and carbon isotope fluxes on the seasonal cycles of CO_2 and $\delta^{13}CO_2$; they were not used for calculating numerical results.

The notation and sign convention introduced above are applied in this manuscript. In brief, $f_{i,j}$ defines a one-way flux from the source reservoir i to the receiving reservoir j and is positive. The isotopic signature of this flux is $\delta^{13}C_{i,j}$. The net flux from reservoir i to reservoir j is $f_{i,j,net}$ and is the difference between the corresponding one-way fluxes, e.g., $f_{i,j,net} = f_{i,j} - f_{j,i}$. $f_{i,j,net}$ is positive if the net flux results in the transfer of mass from i to j .

4 Results

4.1 Seasonal cycles of atmosphere-surface fluxes, C_a , and $\delta^{13}C_a$

The model simulates large seasonal variations in the net land biosphere-atmosphere exchange of CO_2 and $^{13}CO_2$, whereas seasonal variations in ocean-atmosphere fluxes are much smaller (Fig. 1). The seasonality of the Bern3D-LPX carbon fluxes



Table 1. The seasonal cycle amplitude of C_a and $\delta^{13}C_a$ from the standard simulation (Std; $E_{std,standard}$) and observations (Obs) for 19 monitoring sites and the period 1982-2012. The increase over the industrial period is estimated from the difference between the standard simulation and the preindustrial control ($100*(E_{standard} - E_{control})/E_{control}$).

Site	Seasonal Cycle Amplitude of C_a				Seasonal Cycle Amplitude of $\delta^{13}C_a$			
	Standard [ppm]	Observed [ppm]	Std-Obs [ppm]	Increase [%]	Standard [permil]	Observed [permil]	Std-Obs [permil]	Increase [%]
Alert, Nunavut, Canada (82°N)	17.26 ± 0.84	14.82 ± 0.75	2.44	41	0.719 ± 0.035	0.750 ± 0.042	-0.030	8
Barrow, Alaska, US (71°N)	20.10 ± 1.06	15.79 ± 0.75	4.31	37	0.899 ± 0.041	0.822 ± 0.030	0.077	6
Ocean Station M, Norw. (66°N)	17.73 ± 1.14	14.77 ± 0.93	2.96	36	0.763 ± 0.051	0.752 ± 0.028	0.010	4
Cold Bay, Alaska, US (55°N)	14.83 ± 0.80	15.91 ± 1.00	-1.08	39	0.657 ± 0.032	0.847 ± 0.029	-0.190	4
Shemya Island, Alaska, US (53°N)	14.63 ± 0.88	17.03 ± 0.98	-2.40	37	0.655 ± 0.038	0.926 ± 0.029	-0.271	3
Mace Head, Ireland (53°N)	14.65 ± 1.15	13.64 ± 1.74	1.01	42	0.618 ± 0.046	0.726 ± 0.039	-0.107	6
Terceira Island, Portugal (39°N)	11.70 ± 0.86	9.39 ± 1.18	2.31	36	0.497 ± 0.028	0.517 ± 0.036	-0.020	-1
Key Biscayne, Florida, US (26°N)	8.97 ± 0.78	8.17 ± 2.31	0.79	33	0.350 ± 0.031	0.405 ± 0.040	-0.055	-6
Mauna Loa, Hawaii, US (20°N)	8.33 ± 0.30	6.51 ± 0.24	1.82	38	0.328 ± 0.013	0.339 ± 0.028	-0.010	4
Cape Kumukahi, Hawaii (20°N)	9.07 ± 0.39	7.96 ± 0.53	1.11	41	0.358 ± 0.017	0.423 ± 0.028	-0.065	5
Mariana Islands, Guam (13°N)	6.36 ± 0.41	6.11 ± 0.72	0.26	39	0.254 ± 0.019	0.312 ± 0.022	-0.058	3
Ragged Point, Barbados (13°N)	8.00 ± 0.39	7.10 ± 0.45	0.89	38	0.306 ± 0.017	0.332 ± 0.027	-0.026	9
Christmas Island, Kiribati (2°N)	4.68 ± 0.35	2.95 ± 0.38	1.74	77	0.161 ± 0.016	0.129 ± 0.018	0.033	52
Ascension Island, UK (8°S)	3.17 ± 0.41	1.81 ± 0.44	1.37	8	0.134 ± 0.012	0.073 ± 0.016	0.061	-28
Mahe Island, Seychelles (5°S)	3.52 ± 0.41	2.57 ± 0.53	0.95	175	0.145 ± 0.015	0.113 ± 0.021	0.032	63
Tutuila, American Samoa (14°S)	1.29 ± 0.28	0.89 ± 0.30	0.40	51	0.044 ± 0.007	0.020 ± 0.009	0.024	-8
Palmer Station, Antarctica (65°S)	2.60 ± 0.25	1.41 ± 0.19	1.20	21	0.107 ± 0.008	0.037 ± 0.008	0.070	-17
Halley Station, Antarctica (76°S)	2.57 ± 0.15	1.09 ± 0.16	1.48	32	0.103 ± 0.005	0.027 ± 0.007	0.076	-5
South Pole, Antarctica (90°S)	2.06 ± 0.16	1.09 ± 0.11	0.97	20	0.094 ± 0.004	0.033 ± 0.015	0.061	-4

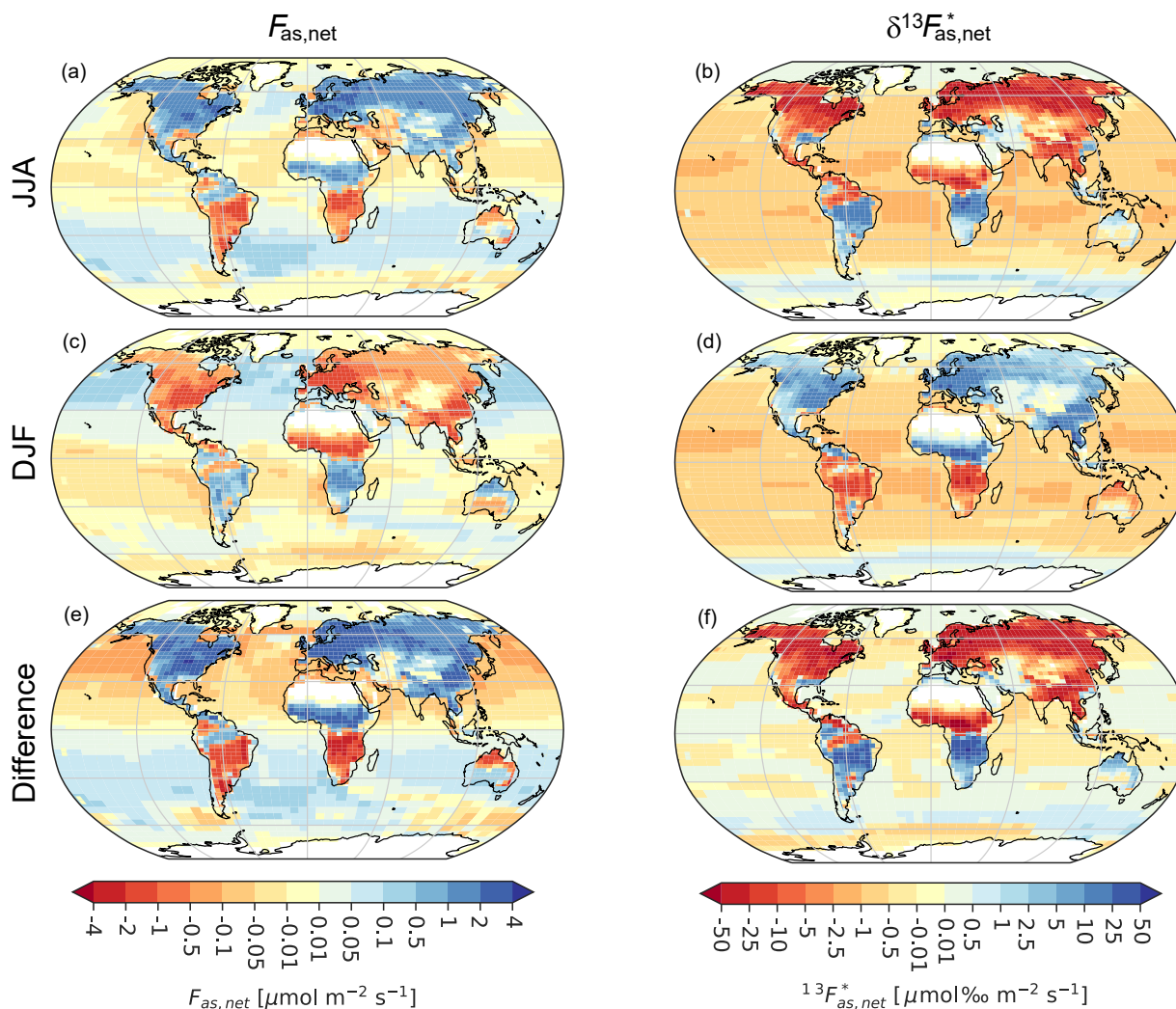


Figure 1. Net seasonal atmosphere-to-surface fluxes. Fluxes are for (a,c,e) carbon and (b,d,f) the $\delta^{13}\text{C}$ -weighted carbon flux, $\delta^{13}f_{as,net}^*$ (see section 3) from the standard simulation (E_{standard}) and averaged over 1982–2012 for (a,b) June, July, August (JJA), (c,d) December, January, February (DJF), and (e,f) JJA minus DJF. Note non-linear color bars with blue colors in panels a to d indicating a lowering in atmospheric CO_2 and $\delta^{13}\text{C}$, respectively.



210 is broadly consistent with estimates of regional air-land carbon flux seasonality from an atmospheric inversion (Gurney et al., 2004) and air-sea flux seasonality from surface ocean pCO₂ observations (Fay et al., 2021), except in the Southern Ocean. The land biosphere model shows the expected uptake of isotopically depleted carbon, resulting in positive $f_{as,net}$ and negative $\delta^{13}f_{as,net}^*$ during the summer and vice versa in winter. On a separate note, the nominal signature of the net carbon flux, $\delta^{13}C_{as,net}$, may be diagnosed by dividing $\delta^{13}f_{as,net}$ by $f_{as,net}$. $\delta^{13}C_{as,net}$ can become very large for small $f_{as,net}$, is hard to
215 interpret, and not used in our approach.

The ocean model shows a negative $\delta^{13}f_{as,net}^*$ in low and mid-latitudes, small modern fluxes in the northern subpolar gyres, and a positive flux in the Southern Ocean in both seasons (Fig. 1). These modern Bern3D fluxes are driven by the atmosphere-ocean isotopic disequilibrium, here defined as the isotopic signature of the atmosphere-to-surface carbon flux minus the signature of the surface-to-atmosphere flux ($\delta_{dis,as}$; Eq. A2), with a negative $\delta_{dis,as}$ in low and mid-latitudes, a small modern
220 disequilibrium in northern high latitudes, and a positive $\delta_{dis,as}$ south of 50°S, consistent with observations (Menviel et al., 2015; Quay et al., 2017; Becker et al., 2018).

The preindustrial air-sea isotopic disequilibrium ($\delta_{dis,as}$; see Appendix A) and $\delta^{13}f_{as,net}^*$ are negative in low- and mid-latitude and positive in high-latitude ocean regions (not shown), mainly driven by the temperature dependency of isotopic fractionation during air-sea exchange and the cycling of marine biological matter (see Fig. 1 of Menviel et al. (2015) for
225 a comparison of Bern3D and LOVECLIM results for the atmosphere-ocean disequilibrium). Fossil fuel emissions cause a negative flux perturbation worldwide, shifting the net isotopic fluxes to more negative values over the industrial period.

Figure 2 compares the mean seasonal cycles of C_a and $\delta^{13}C_a$ from the standard run with measurements from 1982 (Alert: 1985) to 2012 at three sites, and with factorial simulations, where the fluxes of land (green dashed line), the ocean (blue dashed line), and fossil fuel emissions (brown dashed lines) were considered individually (See Table 1 and Supplementary Information,
230 Fig. S1 and S2 for additional sites). For the Northern Hemisphere (NH) sites of Alert (top panels) and Mauna Loa (middle panels), the seasonal variations are dominated by the terrestrial biosphere fluxes, with minor contributions from ocean fluxes and fossil fuel emissions. Note that in contrast to the seasonality of C_a , the seasonality of $\delta^{13}C_a$ does not linearly decompose into the contributions of land, ocean, and fossil fuel emissions. Both the timing and amplitude of the observed seasonal cycle of C_a and $\delta^{13}C_a$ are captured reasonably well by the standard simulation. The simulated $SA(C_a)$ and its interannual variability
235 (IAV) are overestimated compared to observations at Alert (17.3 ± 0.84 ppm vs 14.8 ± 0.75) and Mauna Loa (8.3 ± 0.30 ppm vs 6.5 ± 0.24 ppm). $SA(\delta^{13}C_a)$ matches the observations (ALT: 0.72 ± 0.035 ‰ vs 0.75 ± 0.042 ‰; MLO: 0.34 ± 0.013 ‰ vs 0.33 ± 0.028). Good model-data agreement in the phasing of the seasonal cycle of C_a relative to $\delta^{13}C_a$ is demonstrated for Alert in panel (c), where monthly anomalies in $\delta^{13}C_a$ are plotted versus anomalies in C_a . Both observation and model show hysteresis throughout the year, with the loop rotating clockwise. At Mauna Loa, the rotation direction of the hysteresis loop is
240 clockwise in the simulation and anticlockwise in the observation (panel (f)), but the observed hysteresis is small with offsets of less than 0.03 ‰. The hysteresis arises as the ratio between the rate of change in $\delta^{13}C_a$ versus the rate of change in C_a varies over the year (Keeling et al., 1989; Heimann et al., 1989). This non-linearity in the atmospheric tracer relationship originates from seasonally varying transport in combination with spatially and temporally varying relationships of atmosphere-surface $\delta^{13}C$ to CO₂ flux. For example, the isotopic signature of the growing season net atmosphere-to-land carbon flux $\delta^{13}C_{al,net}$ is

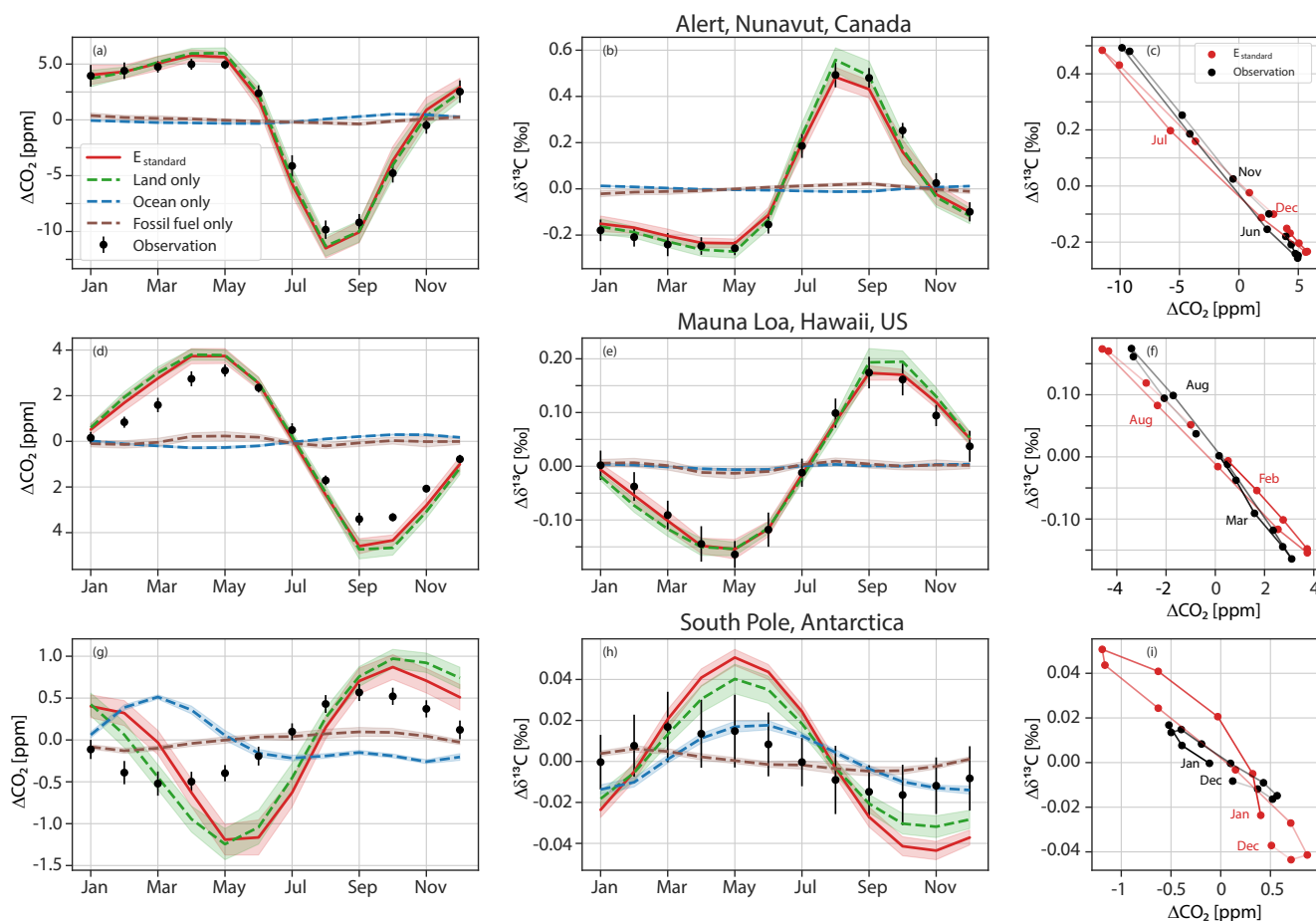


Figure 2. The simulated (red) seasonal cycle of atmospheric CO₂ (left (a,d,g)) and its signature $\delta^{13}\text{C}_a$ (middle (b,e,h)), compared to observations (black dots). In the rightmost panels (c,f,i) the seasonal anomalies (Δ) of CO₂ are plotted against those of $\delta^{13}\text{C}_a$, with lines connecting the monthly values (dots) fading from January to December. Results are for Alert, northern Canada (a,b,c), Mauna Loa, Hawaii (d,e,f), and the South Pole (g,h,i). Simulated values are from transporting in TM3 net fluxes of the Bern3D-LPX standard simulation from all (red, E_{standard}), terrestrial (green, dashed), oceanic (blue, dashed), and fossil sources (brown, dashed). The observational and model anomalies are computed from monthly values between 1982 and 2012 if both the measurements and transport matrices are available. Error bars and shading correspond to the standard deviation from the interannual variability of monthly values.



245 -13.4 ‰ for the northern high-latitude region (>40°N), but only -10.7 ‰ for the region 10°N-40°N and the signal observed at any measurement site results from varying contributions from these and other latitudinal bounds given intraannually varying winds and hence transport.

Results for the South Pole are different than for the NH sites (Fig. 2 (g,h,j)). Neither the timing nor the amplitude of C_a (2.1±0.16 ppm simulated vs 1.1±0.11 ppm observed) and $\delta^{13}C_a$ (0.094±0.004 ‰ vs 0.033±0.015 ‰) agree with observations. $SA(C_a)$ and $SA(\delta^{13}C_a)$ at the South Pole are observed to be 14 and 23 times smaller than at Alert, respectively. The absolute data-model mismatches are therefore not as drastic as the relative mismatches. The disagreement between simulation and observational estimates is also apparent when considering the scatter plot in panel (i). The model shows a complex hysteresis relationship, whereas the observation displays a clockwise loop.

The remote Antarctic sites (South Pole, Palmer, Halley) show an expected relatively larger dependence on the ocean, but the terrestrial contribution still dominates in the model (Figs. 2, S1, S2). The C_a seasonal cycle resulting from atmosphere-ocean flux is shifted by up to six months compared to observations at the South Pole and the other two Antarctic sites (Palmer, Halley; blue lines versus black dots in Fig. S1), pointing to biases in the Bern3D ocean flux. The Bern3D ocean fluxes and their seasonality are broadly comparable to observational estimates over large parts of the ocean (Landschützer et al., 2014; Takahashi et al., 2009; Fay et al., 2021), with ocean CO₂ outgassing in the tropics and uptake in the mid-latitudes during winter (Fig. 1). However, observation-based analyses indicate stronger ocean CO₂ uptake in summer than in winter in the Southern Ocean (Jin et al., 2024; Long et al., 2021; Fay et al., 2021) and the northern subpolar gyres, in contrast to results from Bern3D (Fig. 1) and more complex ocean models (Hauck and Völker, 2015) and several Earth System Models from CMIP5 (Majkut et al., 2014) and CMIP6 (Joos et al., 2023). The simulated amplitude and phasing of the $\delta^{13}C_a$ seasonal cycle resulting from the ocean are broadly in line with observations at the Antarctic sites (Fig. S2). The air-sea isotopic disequilibrium is large in the Southern Ocean and the two-way, air-sea and sea-air, exchange fluxes yield a substantial net isotopic flux, even under low net carbon flux. Temperature-dependent fractionation is higher in winter than summer and the air-sea gas exchange piston velocity, and, in turn, the isotope fluxes are larger under high winds in winter than in summer in the model Southern Ocean, consistent with the observed seasonal phasing of $\delta^{13}C_a$ at the Antarctic sites. Errors in modeled Southern Ocean fluxes are expected to have a minor impact on simulated $SA(C_a)$ and $SA(\delta^{13}C_a)$ at NH sites, where the influence of land fluxes dominates by far (Fig. 2, S1, S2).

Considering all extratropical Northern Hemisphere sites, model-data mismatches are less than 30% for $SA(C_a)$ and $SA(\delta^{13}C_a)$ and their root mean square errors (RMSE) are 2.6 ppm and 0.14 permil, respectively. For the tropical and SH sites, large relative data-model deviations of up to 140% for $SA(C_a)$ and up to 290% for $SA(\delta^{13}C_a)$ are evident, although absolute deviations are less than 1.8 ppm and 0.18 permil and the corresponding RMSEs are 1.2 ppm and 0.05 permil (Table 1).

275 Interannual variability in simulated $SA(\delta^{13}C_a)$ compares reasonably well with observations at sites in the NH subtropics and extratropics (average of the 1- σ standard deviation of 12 sites: 0.031 ‰ in $E_{standard}$ versus 0.031 ‰ in observations) and in the tropics and SH (0.009 vs. 0.013 ‰) (Table 1). Similar agreement between simulated and observation-derived IAV holds for $SA(C_a)$ (NH extratropics: 0.75 vs 0.96 ppm; tropics and SH: 0.29 vs 0.30). This further suggests that the variability in the seasonal amplitude of the underlying carbon and isotope fluxes is reasonably represented by LPX-Bern. The correct simulation

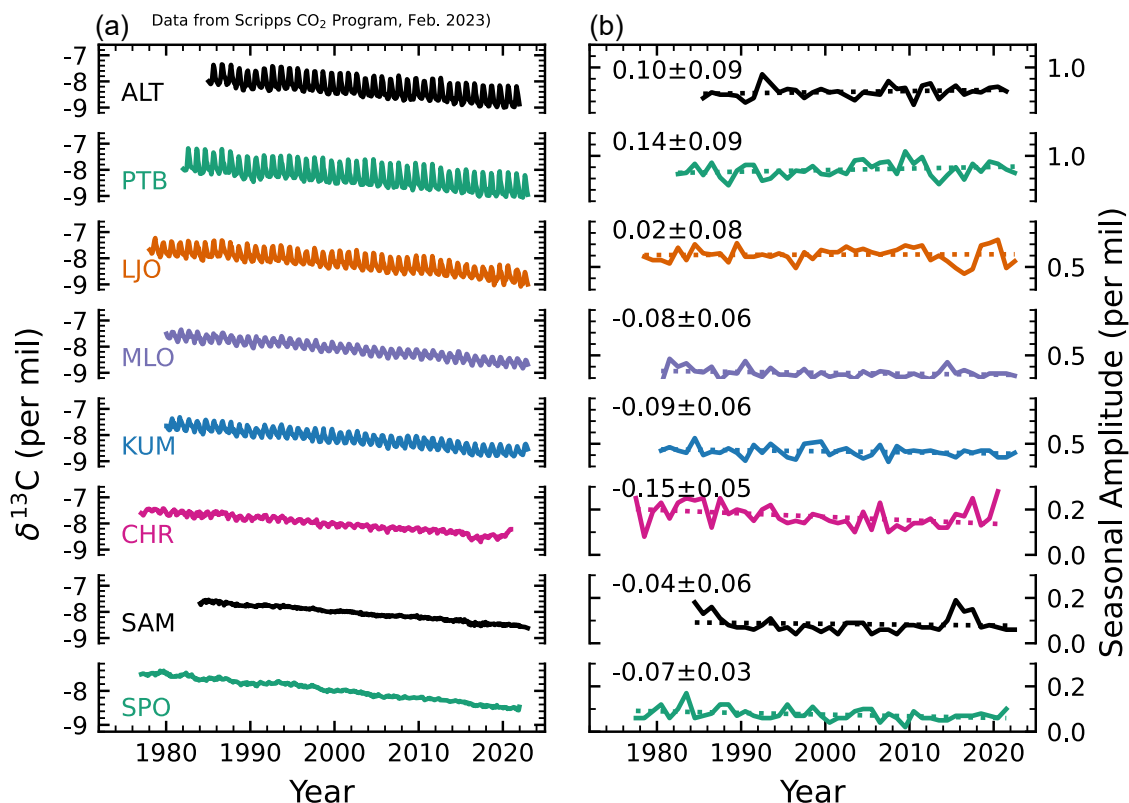


Figure 3. Temporal evolution of $\delta^{13}C_a$ (left) and its seasonal amplitude (right) from data of the Scripps network (Keeling et al., 2001). Gap-filled data provided by Scripps are used for the eight sites. The slope and its standard error from a linear regression through the seasonal amplitude data (dotted) are given in permil/century. Trends are not different from zero based on a two-sided t-test and a significance level of 5%, except at Christmas Island (CHR) and the South Pole (SPO).

280 of variability can be challenging and van der Velde et al. (2013) report too low interannual variability in the annually-integrated isotopic disequilibrium flux for their model.

4.2 Temporal trends in the seasonal cycle amplitude of $\delta^{13}C_a$ and C_a

Temporal trends in $SA(\delta^{13}C_a)$ from the Scripps gap-filled data are not statistically different from zero, except at the tropical site Christmas Island and the South Pole (Fig. 3). Averaging the trends across all 8 sites yields -0.0038 ± 0.026 permil/century (mean \pm 1 sdv of mean) and averaging the trends for the extratropical sites ALT, PTB, and LJO yields $+0.09 \pm 0.06$ permil/century, with both averaged trends not statistically different from zero. The trend for the NH extratropical sites translates into a change in $SA(\delta^{13}C_a)$ of around $5 \pm 3\%$ over the 40-year observational period. Detection of trends in $SA(\delta^{13}C_a)$ may be



Table 2. Temporal trends in the seasonal cycle amplitude of C_a and $\delta^{13}C_a$ from the standard simulation (E_{standard}) and observations for 19 monitoring sites from 1982-2012. Observational data of CO_2 are from the GLOBALVIEW-CO2 product and fitted for the period 1982-2012, while the data for $\delta^{13}C_a$ are from SCRIPPS and fitted as shown in Fig. 3. The seasonal cycle amplitude of a given year is only computed if at least 10 monthly values are available. Number of years included in the trend calculation for $SA(C_a)$ and model-based $SA(\delta^{13}C_a)$ are given in parentheses. The observed trend for C_a is affected by anomalous values at Key Biscayne and is not included. Over the period 1982-2012, significant trends (two-sided t-test at 5% significance) are only found for Alert, Barrow, Ocean Station M, and Mahe Island for observed C_a , for Mariana Islands, Mahe Island, Palmer, Halley, and South Pole for simulated C_a , and Ascension, Mahe Island, and South Pole for simulated $\delta^{13}C_a$. The decadal-scale trends are given per century for better readability.

Site	Trend in Seasonal Cycle Amplitude			
	C_a [ppm/century]		$\delta^{13}C_a$ [permil/century]	
	Observed	Standard	Observed	Standard (years)
Alert, Nunavut, Canada (82°N)	6.5 ± 2.3	5.3 ± 2.7	0.1 ± 0.09	0.02 ± 0.13 (25)
Barrow, Alaska, US (71°N)	9.5 ± 1.9	1.0 ± 3.6	0.14 ± 0.09	-0.09 ± 0.15 (26)
Ocean Station M, Norw. (66°N)	7.2 ± 3.1	7.7 ± 3.9		0.02 ± 0.17 (25)
Cold Bay, Alaska, US (55°N)	1.3 ± 4.4	5.2 ± 4.4		0.10 ± 0.20 (25)
Shemya Island, Alaska, US (53°N)	-0.5 ± 5.3	-0.4 ± 4.9		-0.04 ± 0.22 (21)
Mace Head, Ireland (53°N)	-9.6 ± 14.0	-5.6 ± 4.3		-0.27 ± 0.24 (15)
Terceira Island, Portugal (39°N)	-1.5 ± 6.6	5.7 ± 3.7		0.10 ± 0.17 (14)
Key Biscayne, Florida, US (26°N)		1.5 ± 1.7		0.03 ± 0.07 (25)
Mauna Loa, Hawaii, US (20°N)	-1.6 ± 1.0	0.6 ± 1.4	-0.08 ± 0.06	-0.07 ± 0.05 (26)
Cape Kumukahi, Hawaii (20°N)	-2.1 ± 2.0	2.2 ± 1.6	-0.09 ± 0.06	-0.01 ± 0.06 (26)
Mariana Islands, Guam (13°N)	-2.6 ± 4.8	4.1 ± 1.5		0.08 ± 0.05 (23)
Ragged Point, Barbados (13°N)	-2.1 ± 2.1	-0.3 ± 1.7		-0.06 ± 0.07 (18)
Christmas Island, Kiribati (2°N)	-2.4 ± 1.8	-1.9 ± 1.6	-0.15 ± 0.05	-0.13 ± 0.07 (19)
Ascension Island, UK (7.6°S)	2.7 ± 1.8	-0.6 ± 1.4		-0.15 ± 0.05 (25)
Mahe Island, Seychelles (5°S)	3.7 ± 1.4	6.4 ± 2.3		0.30 ± 0.07 (13)
Tutuila, American Samoa (14°S)	2.2 ± 1.3	-0.5 ± 0.9	-0.04 ± 0.06	-0.04 ± 0.02 (26)
Palmer Station, Antarctica (65°S)	-0.4 ± 0.9	2.4 ± 1.1		0.04 ± 0.04 (23)
Halley Station, Antarctica (76°S)	0.1 ± 1.8	2.9 ± 1.1		0.03 ± 0.04 (17)
South Pole, Antarctica (90°S)	0.7 ± 0.8	2.8 ± 0.7	-0.07 ± 0.03	0.06 ± 0.03 (26)



hampered by interannual-to-decadal variability, short record lengths, and a small $SA(\delta^{13}C_a)$ in comparison to measurement uncertainty and variability as typical at Southern Hemisphere sites. For example, dividing $SA(\delta^{13}C_a)$ by two standard deviations of IAV yields a "signal-to-noise" ratio (Keller et al., 2014) below 2.7 at SH sites and as low as 1.1 at the South Pole and American Samoa (Table 1). Thus, $SA(\delta^{13}C_a)$ would need to roughly double over the observational period for a trend in $SA(\delta^{13}C_a)$ to emerge from the noise of IAV at these two sites. The situation is more favourable for trend detection at NH extratropical sites (Table 1), where the signal-to-noise ratio ranges between 9 and 16 and changes of 6 to 11% in $SA(\delta^{13}C_a)$ would emerge. The Scripps data, including seasonality, are provided as (i) monthly samples, (ii) a fit to these monthly samples, and (iii) the monthly samples but missing values replaced with fitted values. We also used the original, non-gap-filled data and years with at least 9, 10, or 11 monthly values per year in the regression. Trends statistically different from zero are identified for CHR and SPO, whereas the trends at all other sites remain indistinguishable from zero (an exception is MLO when setting the data availability limit to 10 monthly values). For the fitted data, trends are statistically different from zero only at two sites (La Jolla and Christmas Island). In summary, observed temporal trends in $SA(\delta^{13}C_a)$ are small (≤ 0.15 permil/century) and not statistically different from zero (at $p < 0.05$) at individual sites. A significant negative trend is found for the tropical site Christmas Island and detection of trends is difficult at the Southern Hemisphere sites, where $SA(\delta^{13}C_a)$ is small.

The $\delta^{13}C_a$ records of GLOBALVIEW-CO2C13 (2009) span order of a decade and are, therefore, not used for trend detection, although we evaluated trends from the simulations for the GLOBALVIEW sites (Table 2; excluding Key Biscayne). We require at least 10 monthly values for a year to be included in the linear regression. A limitation of our study is that transport matrices are only available for the period 1982 to 2012, limiting the analysis period and direct model-data comparison to three decades only. Simulated trends in $SA(\delta^{13}C_a)$ are small (often less than 0.01‰ per decade) and statistically insignificant (5% level) except at three SH sites (Ascension, Mahe, South Pole), with a small seasonal cycle amplitude. Observed relative trends in $SA(C_a)$ are larger than in $SA(\delta^{13}C_a)$ at northern high latitudes and statistically significant at Alert, Point Barrow, Ocean Station, and Mahe Island but insignificant at all other sites over the 1982-2012 analysis period. Simulated trends in $SA(C_a)$ are insignificant, except at four SH sites and the Mariana Islands.

We compare model (m) and observed (o) slopes (β). Under the null hypothesis of no slope difference, the $T = (\beta_m - \beta_o) / \sqrt{s_{\beta_m}^2 + s_{\beta_o}^2}$ statistic (where s_{β} is the standard error of the β slope estimate) is Student t-distributed (Welch, 1947). Trends are different when the T values are larger than the 0.975 quantile of a t-distribution with ν degrees of freedom ($T > \sim 2$). Modeled and observed trends are different at one site, South Pole, for $SA(\delta^{13}C_a)$ and at one site (Barrow) for $SA(C_a)$. As will become clear in the next section, the largest surface-atmosphere isotope fluxes and temporal changes in these fluxes are simulated in the region north of 40°N. We are therefore interested in quantifying how well the model represents temporal changes in $SA(C_a)$ in this region and over a 40-year period, representative of the $\delta^{13}C_a$ observational record. For the five NH high-latitude sites with more than twenty years of data, uncertainties in the temporal change of $SA(C_a)$ range between 5 and 13% at individual sites over a 40-year period. The average trend in $SA(C_a)$ for these five NH sites (Alert, Barrow, Ocean Station M, Cold Bay, Shemmya Island) is 4.8 ± 1.6 ppm/century (31 ± 10 %/century) from observations and 3.8 ± 1.8 ppm/century (22 ± 11 %/century) from the model. The difference between and the uncertainty in these estimates translates into



a relative change in $SA(C_a)$ of around 4% to 5% over a 40-year period. This suggests that our model chain represents well the observed temporal changes in $SA(C_a)$ in the NH extratropical atmosphere.

Given the mostly insignificant trends at individual sites over the model analysis period 1982-2012, the question arises whether larger trends are detected when considering longer time scales. Century scale trends, or their absence, can be readily estimated in the simulations by comparing SA for the modern period (1982-2012) (E_{standard}) and the control run under preindustrial conditions (E_{control}) (Table 1; solid red versus dashed blue line in Fig. S3 and S4). For C_a , a growth in SA is clearly visible (12.2 ppm to 17.25 ppm at Alert; 6 ppm to 8.3 ppm at Mauna Loa; 1.7 to 2.1 ppm at the South Pole). Across all 19 sites, $SA(C_a)$ has grown by $44\% \pm 35\%$ (mean \pm standard deviation) from 1700 AD to (1982-2010). The growth in $SA(C_a)$ ranges between 33% and 42% across the 12 extratropical NH sites (Table 1).

For $\delta^{13}C_a$, the control simulation exhibits an almost identical SA averaged across all 19 sites ($2\% \pm 16\%$ lower in E_{control} than E_{standard}). Larger deviations are found at individual sites than on average (Fig. S4) with a moderately smaller $SA(\delta^{13}C_a)$ in E_{control} at Alert, almost identical results are found at Mauna Loa and a slightly higher $SA(\delta^{13}C_a)$ is found at the South Pole in E_{control} than E_{standard} . The change in $SA(\delta^{13}C_a)$ from preindustrial (E_{control}) to modern (E_{standard}) range between -6% and 9% across the 12 extratropical NH sites, whereas more diverse results (-28% to + 63%) are simulated at the tropical and SH sites (Fig. S4, Table 1). The modelled industrial period change in $SA(\delta^{13}C_a)$ does not emerge from the noise of variability, except at one tropical (Christmas) and three SH sites (Ascension, Mahe, Palmer). We applied the difference of $SA(\delta^{13}C_a)$ between E_{standard} and E_{control} as signal S and two standard deviations from IAV of E_{standard} (or from the observations) as noise N and requiring $|S|/N > 1$ for the signal to emerge (Keller et al., 2014). The fact that trends in $SA(C_a)$ and the near-zero trends in $SA(\delta^{13}C_a)$ are better identified by difference between the modern and preindustrial periods than by regression over the modern period motivates us to focus on the comparison between E_{standard} vs E_{control} in the remaining result sections.

4.3 Zonal decomposition of seasonal land-biosphere fluxes

4.3.1 Changes in the seasonal amplitude of land-biosphere fluxes and $\delta^{13}C_a$ over the historical period

Next, we address the near-absent temporal trends in $SA(\delta^{13}C_a)$ at NH sites by analyzing the zonally-averaged cumulative growing season flux of $|\delta^{13}f_{al,net}^*|$, i.e., $SA(\delta^{13}f_{al,net}^*)$ (Fig. 4). The northern mid- to high-latitude ecosystem fluxes exhibit the largest seasonal cycle, followed by tropical rain-green forests and savannahs in E_{standard} . This flux pattern contributes to the larger $SA(\delta^{13}C_a)$ at the NH extratropics versus tropical and SH sites. A similar latitudinal flux pattern holds for E_{control} .

Turning to the change over the historical period, $SA(\delta^{13}f_{al,net}^*)$ is 28% larger for the region north of 15°N (30% larger for $>40^\circ\text{N}$, and 20% larger for $15^\circ\text{N}-40^\circ\text{N}$) for E_{standard} than E_{control} . This growth is comparable to the observed increase in atmospheric CO_2 of 32% from pre-industrial to the reference period of 1982-2012. In contrast, E_{control} sometimes exhibits larger $SA(\delta^{13}f_{al,net}^*)$ than E_{standard} in the tropical and SH ecosystems (Fig. 4). Following Eq. 8, the near-proportional growth in the $SA(\delta^{13}f_{al,net}^*)$ and annual mean atmospheric CO_2 in the NH extratropics is consistent with the absence of any major long-term change in $SA(\delta^{13}C_a)$ at extratropical NH sites (Table 1 and Fig. S4). $SA(\delta^{13}C_a)$ and its change at extratropical NH sites is dominated by the large $SA(\delta^{13}f_{al,net}^*)$ in the northern extratropics (Fig. 4) and transport from low latitude regions is

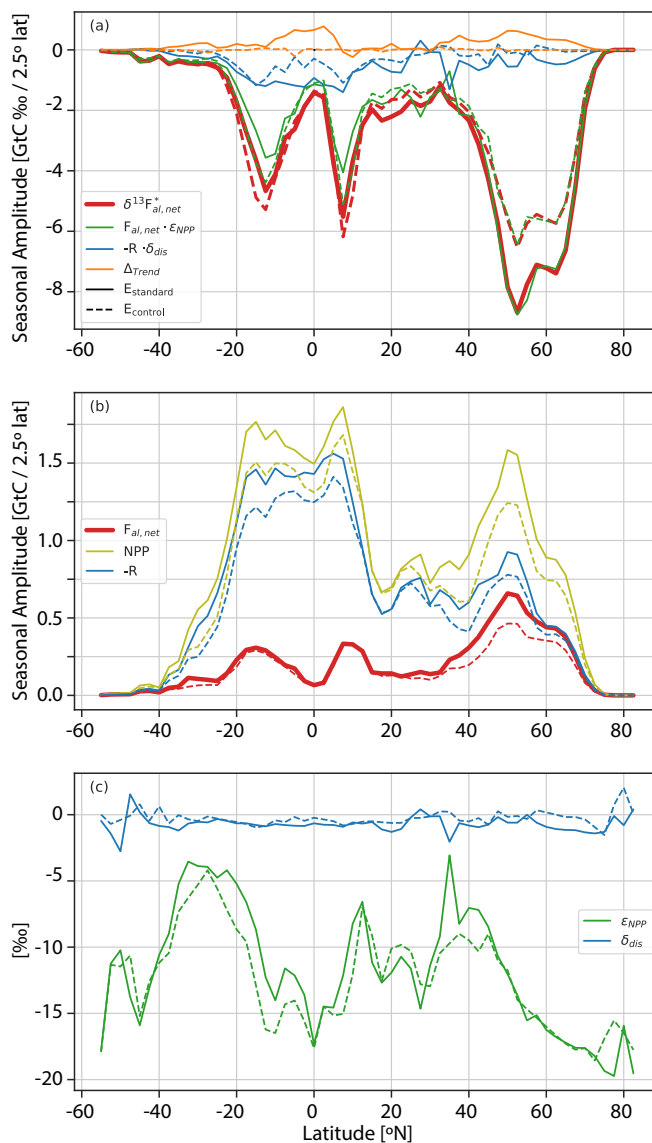


Figure 4. The seasonal amplitude per 2.5° latitude band of the signature-weighted, detrended net atmosphere-land flux $\delta^{13} f_{al,net}^*$ in the period 1982-2012 is shown in panel (a) in red. This quantity is the sum of three constituents seasonal amplitudes (Eq. 9 and Appendix A): Net land-atmosphere flux weighted with photosynthetic fractionation ($f_{al,net} \cdot \epsilon_{NPP}$, green) plus release fluxes weighted with the disequilibrium signature ($R \cdot \delta_{dis,la}$, blue) plus the contribution to the seasonal amplitude by the underlying trend of $\delta^{13} f_{al,net}^*$ (Δ_{trend} , orange) (sign convention: "green+blue+orange=red"). In panel (b), the seasonal amplitudes of (non-detrended) net carbon fluxes are shown. The net atmosphere-land flux ($f_{al,net}$ red) is split in Net Primary Productivity (NPP, olive) and release flux (R , blue). In the bottom panel (c) the corresponding fractionation of photosynthesis ϵ_{NPP} and the disequilibrium signature $\delta_{dis,la}$ is shown. All values are for the period with $\delta^{13} f_{al,net}^*$ smaller than zero (\sim growing season). The y-axis in panel (a) is inverted to illustrate the anticorrelation of $\delta^{13}C$ and carbon fluxes. The results from the standard simulation ($E_{standard}$, solid lines) are compared to the preindustrial control simulation ($E_{control}$, dashed lines).



355 less important. On the other hand, the large extratropical $SA(\delta^{13}f_{al,net}^*)$ influences $SA(\delta^{13}C_a)$ and its temporal changes at lower latitudes. Without this influence, we would, based on Eq. 8, expect a decrease in $SA(\delta^{13}C_a)$ outside the extratropics, given the relative increase in annual mean CO_2 is larger than the increase in $SA(\delta^{13}f_{al,net}^*)$ in these regions.

For CO_2 , the amplitude of the modeled zonally-averaged net atmosphere-to-land CO_2 flux, $SA(f_{al,net})$, shows the largest values in the NH extratropics and a large increase over the historical period of 33% in the region 15°N-90°N (15°N-40°N: 360 26% ; 40°N-90°N: 37%), driven by a larger increase in NPP than release fluxes (R), whereas $SA(f_{al,net})$ is smaller in the tropics and SH and shows hardly any changes from preindustrial ($E_{control}$) to modern ($E_{standard}$) south of 20°N.

4.3.2 The coupling between the seasonal amplitude of C_a and $\delta^{13}C_a$

$SA(C_a)$ and $SA(\delta^{13}C_a)$ are partly coupled by the underlying carbon fluxes. The question arises to which extent $SA(\delta^{13}C_a)$ holds information independent from $SA(C_a)$. We decompose $\delta^{13}f_{al,net}^*$ in a contribution linked to the net atmosphere-to-land 365 carbon flux, $f_{al,net}=NPP-R$, and an isotopic disequilibrium flux (see Appendix A and section 3 for notation; $f_{al,net}$ is positive for a flux into the land biosphere):

$$\delta^{13}f_{al,net}^* = \underbrace{(NPP - R)}_{f_{al,net}} \cdot \varepsilon_{NPP} - R \cdot \underbrace{(\delta^{13}C_R - \delta^{13}C_{NPP})}_{\delta_{dis,la}}. \quad (9)$$

NPP is the net primary productivity of all plants within a grid cell. R is the sum of all land biosphere release fluxes to the atmosphere, such as those from heterotrophic respiration, fire, mortality, and product pools, except autotrophic respiration. 370 $\delta^{13}C_R$ is the signature of R and $\delta^{13}C_{NPP}$ is the signature of NPP, with ε_{NPP} (or ε_{al}) representing the (flux-weighted) fractionation by NPP. The difference in signatures of R and NPP is the isotopic disequilibrium, $\delta_{dis,la}$. Eq. 9, together with Eqs. 7 and 8, provide insights into the driving factors for the seasonal amplitudes. Putting the ocean aside (Heimann et al., 1989), $SA(C_a)$ is driven by the spatio-temporal pattern of $(NPP-R)$, whereas $SA(\delta^{13}C_a)$ is additionally influenced by seasonal variations in ε_{NPP} , and the disequilibrium flux ($R \cdot \delta_{dis,la}$).

375 The decomposition of zonally-averaged $SA(\delta^{13}f_{al,net}^*)$ into the amplitude of constituent fluxes and their isotopic signatures is displayed in Figure 4 and Table S1. On the global average, $SA(f_{al,net} \cdot \varepsilon_{NPP})$, the amplitude of the net atmosphere-land flux ($f_{al,net}$) weighted with the signature of photosynthesis (ε_{NPP}), contributes with a fraction of 90% to $SA(\delta^{13}f_{al,net}^*)$ for both $E_{standard}$ and $E_{control}$. For the region north of 40°N, $SA(-R \cdot \delta_{dis,la})$, the amplitude of the disequilibrium flux, contributes only 7% to $SA(\delta^{13}f_{al,net}^*)$ in $E_{standard}$ and is almost negligible for $E_{control}$ (2%). This small contribution of the disequilibrium 380 flux ($-R \cdot \delta_{dis,la}$) relative to the net flux ($f_{al,net} \cdot \varepsilon_{NPP}$; Eq. 9) arises as the seasonal amplitude of the carbon release flux R is similar in magnitude to that of the net land carbon uptake $f_{al,net}$ in the northern extratropics (blue vs red lines in Fig. 4b) while the disequilibrium $\delta_{dis,la}$ is an order of magnitude smaller than ε_{NPP} (Fig. 4c). Thus in LPX, $SA(\delta^{13}C_a)$ is dominated by the growing season net carbon uptake flux in northern high-latitudes, suggesting that $SA(\delta^{13}C_a)$ holds little information on the isotopic disequilibrium at high latitude sites. In contrast, the contribution by the disequilibrium flux $SA(-R \cdot \delta_{dis,la})$ and 385 by the net carbon flux $SA(f_{al,net} \cdot \varepsilon_{NPP})$ are near-equal in the tropics (10°S-10°N) and the SH (Fig. 4, Table S1). Note that in $E_{control}$, SA of the disequilibrium flux and the disequilibrium between photosynthesis and respiration (Eq. 9 and Fig. 4),



albeit smaller than in E_{standard} , are not negligible due to the lagged response of the respiration signatures to natural changes in ε_{NPP} . A small contribution (Δ_{trend}) to the isotopic flux seasonality in E_{standard} arises from the secular increase in flux (Fig. 4; see Appendix A). $SA(\text{NPP})$ and $SA(R)$ increase from preindustrial to modern not only in northern ecosystems but also in the tropics (Fig. 4b). $SA(\text{NPP}-R)$ increases in the NH extratropics but does hardly change south of 20°N .

The zonal variation in (growing season) photosynthetic fractionation ε_{NPP} is mainly due to differences in vegetation composition, with C4 plants having considerably lower photosynthetic fractionation than C3 plants (Fig. 4c). Land use and the evolving distribution of C3 and C4 crops are prescribed in the model and C4 grasses are more prevalent than C3 grasses in low-latitude dryland ecosystems. Accordingly, maxima in flux-weighted, zonal-mean ε_{NPP} are simulated at 35°N , 12°N , and broadly around 30°S . Minima are simulated for the C3-dominated high-latitude ecosystems and tropical rain forest zone. In E_{standard} ε_{NPP} is generally less negative than in E_{control} and increased by 1.18‰ (9% in relative units) on the global average ($SA(\text{NPP})$ -weighted) mainly due to the increase in the prevalence of C4 plants. To estimate the influence of the increase in C4 prevalence on global mean ε_{NPP} (but not on global GPP), we run a factorial simulations, E_{C3} , with the fractionation formulation for all C4 plants replaced by those for C3 plants. The difference between E_{standard} and E_{C3} , i.e., the change in fractionation attributable to C4 plants, amounts to about 1.5‰ on global average (1982-2012 versus 1720-1750) (Fig. S5). The disequilibrium signature $\delta_{\text{dis},la}$ is closer to zero for the control than the standard simulation. This is expected because the signal from the atmospheric ^{13}C Suess effect in R is delayed relative to NPP by vegetation, soil, and product pool lifetimes, leading to a disequilibrium with respect to the production signature.

5 Discussion

5.1 Growth in seasonal cycle amplitudes: implications for stomatal conductance and water use

The seasonal amplitude of CO_2 ($SA(C_a)$) is observed to grow over time depending on location (Bacastow et al., 1985; Barlow et al., 2015; Piao et al., 2018) and driven by changes in the seasonality of net land carbon uptake (Graven et al., 2013; Forkel et al., 2016). The growth is captured by our model and simulated and observations-based trends generally agree within uncertainties at individual stations. Averaging the signals across northern high-latitude sites ($>40^\circ\text{N}$), yields relatively small uncertainties in data and model slopes and their difference, corresponding to a change in seasonal amplitude of 5% ($1-\sigma$) over a 40-year period. Corresponding uncertainties and data-model mismatches in slopes are up to 21% for the individual high latitude sites. The good data-model agreement for the averaged trend suggests that our model chain broadly captures the influence of trends in the seasonal cycle of net land carbon uptake on trends in $SA(C_a)$ and $SA(\delta^{13}\text{C}_a)$ at northern sites.

Previous studies show northern ecosystems progressively taking up more carbon during the growing season (Graven et al., 2013; Forkel et al., 2016; Piao et al., 2018; Bastos et al., 2019). For example, Bastos et al. (2019) find a positive trend in $SA(f_{\text{al},\text{net}})$ north of 40°N and small or no growth in $SA(f_{\text{al},\text{net}})$ between 25°N and 40°N . Consistent with these studies, the seasonal cycle amplitude of NPP and the terrestrial release flux R is simulated by LPX-Bern to increase over the industrial period in both hemispheres, but the growing season net carbon uptake ($SA(\text{NPP}-R)=SA(f_{\text{al},\text{net}})$) is only increasing north of $\sim 30^\circ\text{N}$ (Fig. 4b).



420 For $\delta^{13}C_a$, the observations from the (GLOBALVIEW-CO2C13, 2009) and Scripps products do not show a statistically significant change of $SA(\delta^{13}C_a)$ at most sites with more than 20 years of data (Fig. 3). This is consistent with Gonsamo et al. (2017) who did not detect a temporal trend in $SA(\delta^{13}C_a)$ and seasonal phasing by fitting Scripps daily flask data from the four sites Alert, Point Barrow, La Jolla, and Mauna Loa. Modeled changes in $SA(\delta^{13}C_a)$ yield no clear trend in the standard case over the simulation period 1982 to 2012, consistent with the observations. Further, $SA(\delta^{13}C_a)$ is in general very similar for the
425 preindustrial control and the standard case at the NH sites (Table 1; dashed blue vs red line in Supplementary Fig. S4), again consistent with the statistically insignificant trend in the observations.

Theoretical considerations imply no trend in $SA(\delta^{13}C_a)$ for a proportional growth in the seasonality of net atmosphere-surface isotope flux ($\sim SA(\delta^{13}f_{al,net}^*)$) and in background atmospheric CO_2 (see Eq. 8 section 3). Both parameters increased by about 30% over the industrial period over northern ecosystems ($>40^\circ N$). The growth in $SA(\delta^{13}f_{al,net}^*)$ is primarily driven
430 by the increase in growing season net carbon uptake ($SA(f_{al,net})$) at northern latitudes. We suggest that the near-proportional growth in $SA(\delta^{13}f_{al,net}^*)$ and in background atmospheric CO_2 is mainly responsible for the statistically insignificant trend in $SA(\delta^{13}C_a)$ at high northern latitude sites, and contributing to the statistically insignificant trend in $SA(\delta^{13}C_a)$ at other NH sites via atmospheric transport.

Factorial simulations, with an individual forcing kept at preindustrial, show small individual contributions by climate change,
435 fossil emissions, and land use to the industrial period growth in $SA(\delta^{13}C_a)$ at northern extratropical sites (Fig. S3 and S4). This suggests that the statistically insignificant trend in $SA(\delta^{13}C_a)$ at northern extratropical sites is not caused by offsetting impacts of climate change versus increasing CO_2 . Fossil fuel emissions cause an increase and land use change a reduction in $SA(\delta^{13}C_a)$ at low latitude and southern sites (Fig. S3 and S4). We attribute the dampening influence of land use change to the replacement of C4 plants by C3 crops causing a general shift in the fractionation during photosynthesis to less negative values
440 south of $\sim 45^\circ N$ (Fig. 4c). This damping influence highlights the importance of considering spatiotemporal variations in C3 and C4 plant distributions when analyzing $\delta^{13}C_a$.

Our results hold implications for carbon and water fluxes, and evaporative cooling. The good agreement between observations and model results for $SA(\delta^{13}C_a)$ and its temporal trend provides implicit support for regulation of stomatal conductance by C3 plants towards a constant ratio of the CO_2 mole fraction in the leaf intercellular space (c_i) and ambient atmospheric air
445 (c_a) on the continental scale. Following Farquhar (1989), the fractionation for C3 photosynthesis and NPP (ε_{NPP}) is proportional to c_i/c_a :

$$\varepsilon_{NPP} = a + (b - a) \cdot \frac{c_i}{c_a}, \quad (10)$$

with a (4.4), and b (27) being constants. Two contrasting scenarios are published for the regulation of leaf stomatal conductance for C3 plants. First, many site studies (Voelker et al., 2016; Saurer et al., 2014; Kauwe et al., 2013; Peñuelas et al., 2011; Frank
450 et al., 2015; Keller et al., 2017) suggest a regulation of stomatal conductance towards a constant c_i/c_a and, hence, c_i to grow proportional to c_a . An absent temporal trend in c_i/c_a translates into an absent trend in ε_{NPP} , and vice versa (Eq. 10). Focusing on regions north of $>40^\circ N$, where carbon fluxes are largest and C3 plants dominate, LPX-Bern simulates a small role of isotopic disequilibrium fluxes and a dominant influence of net atmosphere-surface fluxes on $SA(\delta^{13}C_a)$ (Fig. 4, green vs



blue lines). Importantly, LPX-Bern simulates small temporal changes in the (flux-weighted) fractionation of the zonally and
455 seasonally integrated NPP at northern sites (Fig. 4c, green lines) and a stomatal regulation towards constant c_i/c_a . In turn,
the good model-data agreement in the temporal trends of $SA(C_a)$ and $SA(\delta^{13}C_a)$ imply consistency with the observational
evidence for this scenario towards constant c_i/c_a .

In contrast, Battipaglia et al. (2013) and Keenan et al. (2013) suggest a regulation of stomatal conductance towards a constant
 c_i and a decreasing ratio c_i/c_a under rising CO_2 . Evaluating Eqs. 10 for 1980-2022, the period with $\delta^{13}C_a$ measurements,
460 yields a decrease in ϵ_{NPP} of 15% (-3.0 to -3.8 ‰) for an initial c_i/c_a ratio in the range of 0.7 to 0.9 and constant c_i . We argue
that the good observation-model agreement in the simulated trends in $SA(C_a)$ implies that the influence of the simulated net
atmosphere-land carbon flux is realistic and $SA(\delta^{13}C_a)$ would decrease if ϵ_{NPP} decreases. A decrease in $SA(\delta^{13}C_a)$ of 15%
would emerge from the noise of variability at individual northern sites. Taken together, we suggest that the scenario towards
constant c_i/c_a is consistent with the observations whereas the scenario towards constant c_i appears less likely. However,
465 uncertainties remain and our conclusions for the two scenarios of stomatal regulation await confirmation by other modelling
studies.

The two scenarios imply large differences in water fluxes (Knauer et al., 2017). The intrinsic water use efficiency (iWUE),
the ratio between assimilation of CO_2 by photosynthesis (A) and conductance of CO_2 (g), is, as ϵ_{NPP} , a function of c_i and c_a :

$$iWUE = \frac{A}{g} = c_a \cdot \left(1 - \frac{c_i}{c_a}\right). \quad (11)$$

470 iWUE would have increased from 1980 to 2022 by 23% for c_i/c_a constant, but by 77 to 231% for c_i constant, assuming an
initial c_i/c_a of 0.7 to 0.9. In the latter scenario, stomatal conductance and, correspondingly, water loss per stomatal pore, would
have decreased strongly over the last decades.

5.2 Seasonality: C_a versus $\delta^{13}C_a$ and isotopic disequilibrium

Observations of $\delta^{13}C_a$ seasonality provide different, complementary information compared to observations of C_a seasonality.
475 As discussed above, the model results suggest that the additional information of $SA(\delta^{13}C_a)$ compared to $SA(C_a)$ is in the
magnitude of ϵ_{NPP} at northern high-latitude sites. The contribution of the isotopic disequilibrium flux, indicative of the transit
time of carbon through the land biosphere, plays a relatively small role in the northern extratropics, given the large growing
season net carbon uptake flux in this region (Fig. 4). In contrast, for tropical and SH ecosystems, the terrestrial isotopic
disequilibrium flux plays a large role (blue versus green line in Fig. 4a), at least in our model. However, the seasonality
480 of $\delta^{13}C_a$ and C_a at the tropical background monitoring sites analyzed in this study is strongly influenced by long-range
transport, adding uncertainty to the interpretation of seasonal signals. Further, we have limited understanding of net ecosystem
exchange in the tropics, and uptake and release fluxes may cancel largely in the evergreen rain forest limiting the value of
seasonal analyses in this biome. Monitoring C_a and $\delta^{13}C_a$ over tropical and SH land regions could potentially provide valid
information to disentangle NPP, respiration, and net carbon fluxes. Ideally, seasonally-resolved observations are taken in air
485 masses influenced primarily by regional land biosphere fluxes, thereby minimizing uncertainties from long-range transport,
and interpreted with the help of atmospheric transport and land biosphere models (Botía et al., 2022). For example, the data



may be assimilated into atmospheric transport models applied in inverse mode to infer surface carbon and isotope fluxes or into isotope-enabled land biosphere models, combined with atmospheric transport, to optimize parameters governing modelled carbon and isotope fluxes (Peylin et al., 2016; Castro-Morales et al., 2019).

490 While the influence of the gross exchange flux and the isotopic disequilibrium on $\delta^{13}\text{C}_a$ seasonality is modeled to be small at northern sites for today, it remains to be explored how global warming will change these parameters, e.g., due to changes in fire frequency and tree mortality, and affect $\delta^{13}\text{C}_a$ and the information provided by continued $\delta^{13}\text{C}_a$ observations. We may also expect different disequilibrium fluxes and, in turn, $\delta^{13}\text{C}_a$ seasonality if the global carbon sink is driven by a stimulation of NPP, e.g., by CO_2 fertilization (Walker et al., 2021) as in LPX-Bern, versus a change in tree longevity (Bugmann and Christof, 495 2011; Körner, 2017). It remains to investigate, e.g., by applying perturbed parameter ensembles and sensitivity simulations, whether such differences indeed significantly affect $\delta^{13}\text{C}_a$ seasonality.

The role of isotopic disequilibrium fluxes depends on the timescales considered. Analyses of the global budget of annual-mean atmospheric $\delta^{13}\text{C}(\text{CO}_2)$ (Keeling et al., 1989; Francey et al., 1995; Joos and Bruno, 1998; Trudinger et al., 2002; van der Velde et al., 2013) indicate that the emissions of isotopically-light carbon from fossil fuel burning are primarily balanced by a 500 reduction in the atmospheric inventory and ocean and land disequilibrium fluxes, leaving a relatively small role for the isotopic flux associated with the net ocean and land carbon sink. Ocean and land fluxes are about equally important for the removal of the fossil fuel $\delta^{13}\text{C}(C_a)$ perturbation. For the seasonality of $\delta^{13}\text{C}(C_a)$, our results confirm that the land fluxes exert a dominant influence compared to ocean fluxes at NH sites and we find, on the global average, that the disequilibrium flux contributes a small fraction to the seasonal amplitude of the net land isotope flux.

505 On a technical note, transporting simulated ^{13}C fluxes is not without challenges. The definition of the δ -notation can pose numerical difficulties when net ^{12}C fluxes are close to zero. We find that transporting signature-weighted total carbon fluxes is the most reliable method for arriving at local $\delta^{13}\text{C}_a$. Similarly, seemingly small errors in the model representation of gross fluxes and mass balances, can become critical when considering net surface-to-atmosphere fluxes.

6 Conclusions

510 In conclusion, we explored the global-scale mechanisms driving the observed seasonal cycle of atmospheric $\delta^{13}\text{C}(\text{CO}_2)$ and CO_2 at 19 monitoring sites using atmosphere-surface fluxes from the Bern3D-LPX Earth System Model of Intermediate Complexity and fossil emissions in combination with transport matrices from the TM3 atmospheric transport model. We find good data-model agreement at northern and tropical sites. No significant trends are detected nor modeled in the seasonal cycle amplitude of $\delta^{13}\text{C}(\text{CO}_2)$ at most monitoring sites, in contrast to the positive trends in the seasonal amplitude of CO_2 . We attribute 515 the statistically insignificant trend in the seasonal amplitude of $\delta^{13}\text{C}(\text{CO}_2)$ to a near-equal percentage increase in the growing season net carbon uptake and isotope flux and the background atmospheric CO_2 in the northern extratropical land regions. Over the industrial period and at low-latitude and SH sites, land use change has a dampening influence on $\delta^{13}\text{C}_a$ seasonality through the replacement of C3 plants by C4 crops. Modeled isotopic disequilibrium fluxes have a small influence on the seasonal signal of $\delta^{13}\text{C}(\text{CO}_2)$ at NH sites, but play an important role in tropic and SH ecosystems, suggesting that monitoring



520 the $\delta^{13}\text{C}_a$ seasonality over tropical and SH land would provide valuable information on gross carbon exchange fluxes and the
time scales of carbon turnover in the land biosphere. Our results, based on a single model chain, provide implicit support for a
regulation of the stomatal conductance of C3 plants towards a constant c_i/c_a on biome scales and intrinsic water use efficiency
to grow proportionally to atmospheric CO_2 over recent decades with implications for carbon and water fluxes. More generally,
the results suggest that observations of the $\delta^{13}\text{C}_a$ seasonal cycle offer highly useful information on carbon and water cycle
525 processes. We recommend to apply seasonally-resolved $\delta^{13}\text{C}_a$ observations as a novel constraint for land biosphere models
used to simulate the terrestrial sink of anthropogenic carbon and land use emissions. Future studies may employ an ensemble
of isotope enabled models and perturbed parameter ensembles to elucidate whether our findings are robust and which models
or process assumptions are compatible or incompatible with $\delta^{13}\text{C}_a$ data for improved projections of atmospheric CO_2 and
global warming.

530 *Code and data availability.* The data from the Scripps CO_2 program are available here: https://scrippsco2.ucsd.edu/data/atmospheric_co2/.
The GLOBALVIEW data from the Global Monitoring Laboratory were downloaded here: <https://gml.noaa.gov/ccgg/globalview/>. The data
displayed in the Figures will be made freely available at Zenodo or a similar site when the manuscript is accepted. For the review process the
data and plotting scripts are available as a download: <https://cloud.climate.unibe.ch/s/g9qrit7KDRnrLp>

Appendix A: Decomposition of $\delta^{13}f_{as,net}^*$ and the calculation of seasonal amplitudes

535 We reformulate the net isotope flux in terms of net and gross carbon fluxes, isotopic fractionation, and isotopic disequilibrium
(e.g., Mook (1986); Joos and Bruno (1998)) to diagnose their influence on the seasonal cycles.

The fractionation for a gross flux, e.g., from the atmosphere to the surface, is:

$$\varepsilon_{as} \cong (\delta^{13}\text{C}_{as} - \delta^{13}\text{C}_a), \quad (\text{A1})$$

540 with $\delta^{13}\text{C}_{as}$ the signature of the gross flux from a to s (f_{as}) and $\delta^{13}\text{C}_a$ the signature of the source. The isotopic disequilibrium
(or difference) between atmosphere-surface gross fluxes is:

$$\delta_{dis,sa} = -\delta_{dis,as} = (\delta^{13}\text{C}_{sa} - \delta^{13}\text{C}_{as}) \quad (\text{A2})$$

The net carbon and isotope fluxes are differences between gross fluxes:

$$f_{as,net} = f_{as} - f_{sa} \quad (\text{A3})$$

$$545 \delta^{13}f_{as,net}^* = f_{as} \cdot (\delta^{13}\text{C}_{as} - \delta^{13}\text{C}_a) - f_{sa} \cdot (\delta^{13}\text{C}_{sa} - \delta^{13}\text{C}_a) \quad (\text{A4})$$

Rearranging yields:

$$\delta^{13}f_{as,net}^* = f_{as,net} \cdot \underbrace{(\delta^{13}\text{C}_{as} - \delta^{13}\text{C}_a)}_{\varepsilon_{as}} - f_{sa} \cdot \underbrace{(\delta^{13}\text{C}_{sa} - \delta^{13}\text{C}_{as})}_{\delta_{dis,sa}} \quad (\text{A5})$$



For the land biosphere (index l), it follows from Eqs. A3 and A5:

$$f_{al,net} = \text{NPP} - R \quad (\text{A6})$$

550

$$\delta^{13} f_{al,net}^* = f_{al,net} \cdot \varepsilon_{\text{NPP}} - R \cdot \delta_{dis,la}, \quad (\text{A7})$$

with:

$$\delta_{dis,la} = \delta^{13} C_R - \delta^{13} C_{\text{NPP}} \quad (\text{A8})$$

555 NPP is the net primary productivity of all plants within a grid cell. R is the sum of all release fluxes to the atmosphere, such as those from heterotrophic respiration, fire, mortality, and product pools. $\delta^{13} C_R$ is the signature of R and $\delta^{13} C_{\text{NPP}}$ is the signature of NPP, with ε_{NPP} (or ε_{al}) representing the (flux-weighted) fractionation by NPP. Here, as in LPX-Bern, we have assumed that the uptake difference between gross primary production (GPP) and NPP is released on short time scales and without further carbon isotope fractionation.

560 The seasonal amplitudes of $\delta^{13} f_{al,net}^*$ and its components are calculated as follows. The time series of $\delta^{13} f_{al,net}^*$ is detrended and normalized to zero. The trend is computed by a rolling 12-month mean of $\delta^{13} f_{al,net}^*$. Then, the resulting trend curve is subtracted from $\delta^{13} f_{al,net}^*$ (disregarding the first and last 6 months of the original series) to get a detrended curve. Finally, the detrended curve is normalized by subtracting its period mean. Δ_{trend} (e.g., in units of mol permil $\text{yr}^{-1} \text{m}^{-2}$) is the difference between $\delta^{13} f_{al,net}^*$ after and before this detrending and normalizing procedure. We define a seasonal mask to compute seasonal amplitudes of fluxes and their signatures. For each model year, we identify months in which detrended $\delta^{13} f_{al,net}^*$ is negative or equal to zero (roughly corresponding to the growing season). The sum of fluxes of these months is then termed the "seasonal amplitude" in a given year. For $\delta^{13} f_{al,net}^*$, this procedure is consistent with considering the difference between maximum and minimum values of the detrended cumulative sum of $\delta^{13} f_{al,net}^*$. Accordingly, the seasonal amplitudes of the component fluxes contributing to $\delta^{13} f_{al,net}^*$ are computed by summation over months where $\delta^{13} f_{al,net}^*$ is less or equal to zero within a given year. Component fluxes are $[(\text{NPP}-R) \cdot \varepsilon_{\text{NPP}}]$, $[R \cdot \delta_{dis,la}]$, $[\Delta_{trend}]$, and, further, $[\text{NPP}]$, $[R]$, and $[\text{NPP}-R]$ (Fig. 4). These 570 component fluxes are not detrended to readily calculate the signatures $\delta_{dis,la}$ and ε_{NPP} by division of the seasonal amplitude isotopic flux with the corresponding seasonal amplitude carbon flux.

575 We note that the annual climatological mean values of the isotopic disequilibrium ($\delta_{dis,la}$), the net carbon flux ($f_{al,net}$), and the net isotopic flux ($\delta^{13} f_{al,net}^*$) vanish by definition for the preindustrial equilibrium. However, this does not hold for their seasonal amplitudes. Further, detrending $\delta^{13} f_{al,net}^*$ before the computation of its seasonal amplitude is consistent with the calculation of the C_a and $\delta^{13} C_a$ seasonal amplitude from the detrended atmospheric time series.

The seasonal cycles of C_a or $\delta^{13} C_a$ are computed from observations and the TM3 results using the following procedure for either C_a or $\delta^{13} C_a$, respectively. Months with missing values in either the observation or the TM3 simulation are masked in the TM3 and observational time series. Then the time series are detrended using a 12-month rolling mean and the overall mean of the series is set to zero to get for year, y , and month, m , seasonal anomalies $\Delta C_a(y, m)$ and $\Delta \delta^{13} C_a(y, m)$. Finally, the



580 period means for each calendar month, $\overline{\Delta C_a(m)}$ and $\overline{\Delta \delta^{13}C_a(m)}$, are computed by averaging over all corresponding monthly values. Additionally, the standard deviation is computed for each calendar month to inform about the interannual variability of the seasonality. The period-mean SA is computed as the difference between the month with the highest ($\overline{m_{\max}}$) and lowest ($\overline{m_{\min}}$) value in $\overline{\Delta C_a(m)}$ and $\overline{\Delta \delta^{13}C_a(m)}$, respectively. For individual years, we computed SA by difference from the extreme monthly values of each year.

585 *Author contributions.* FJ and SL wrote the manuscript with inputs from SZ. SL performed all model runs and FJ the statistical analyses. SL and FJ produced the figures and tables.

Competing interests. The authors declare to have no competing interests

Acknowledgements. This project has received funding from the European Union's Horizon 2020 research and innovation programme under grant agreement No 821003 (project 4C, Climate-Carbon Interactions in the Current Century) and by the Swiss National Science Foundation (project #200020_200511). The work reflects only the authors' view; the European Commission and their executive agency are not responsible for any use that may be made of the information the work contains. We thank the researchers of the Cooperative Atmospheric Data Integration Project, NOAA ESRL, Boulder, Colorado, and of the Scripps CO₂ program for making their CO₂ and $\delta^{13}C$ data freely available and Martin Heimann for suggesting to plot seasonal anomalies of CO₂ versus those of $\delta^{13}C$. A special thanks goes to Christoph Köstler for providing the TM3 transport matrices and to Aurich Jeltsch-Thömmes for help with Bern3D.

590



595 References

- Andres, R., Marland, G., Boden, T., and Bischof, S.: Carbon dioxide emissions from fossil fuel consumption and cement manufacture, 1751-1991, and an estimate of their isotopic composition and latitudinal distribution, in: *The Carbon Cycle*, edited by Schimmel, D., pp. 53–62, 2000.
- Andres, R., Boden, T., and Marland, G.: Monthly Fossil-Fuel CO₂ Emissions: Mass of Emissions Gridded by One Degree Latitude by One Degree Longitude - 2016, <https://doi.org/10.3334/CDIAC/FFE.MONTHLYMASS.2016>, 2009a.
- Andres, R., Boden, T., and Marland, G.: Monthly Fossil-Fuel CO₂ Emissions: Isomass of Emissions Gridded by One Degree Latitude by One Degree Longitude, <https://doi.org/10.3334/CDIAC/FFE.MONTHLYISOMASS.2016>, 2009b.
- Andres, R., Boden, T., and Marland, G.: Annual Fossil-Fuel CO₂ Emissions: Global Stable Carbon Isotopic Signature, <https://doi.org/10.3334/CDIAC/FFE.DB1013.2017>, 2017.
- 605 Bacastow, R. B., Keeling, C. D., and Whorf, T. P.: Seasonal amplitude increase in atmospheric CO₂ concentration at Mauna Loa, Hawaii, 1959-1982, *Journal of Geophysical Research: Atmospheres*, 90, 10 529–10 540, <https://doi.org/10.1029/JD090iD06p10529>, 1985.
- Ballantyne, A. P., Miller, J. B., and Tans, P. P.: Apparent seasonal cycle in isotopic discrimination of carbon in the atmosphere and biosphere due to vapor pressure deficit, *Global Biogeochemical Cycles*, 24, 1–16, <https://doi.org/10.1029/2009GB003623>, 2010.
- Barlow, J. M., Palmer, P. I., Bruhwiler, L. M., and Tans, P.: Analysis of CO₂ mole fraction data: First evidence of large-scale changes in CO₂ uptake at high northern latitudes, *Atmospheric Chemistry and Physics*, 15, 13 739–13 758, <https://doi.org/10.5194/acp-15-13739-2015>, 2015.
- 610 Bastos, A., Ciais, P., Chevallier, F., Rödenbeck, C., Ballantyne, A. P., Maignan, F., Yin, Y., Fernández-Martínez, M., Friedlingstein, P., Peñuelas, J., Piao, S. L., Sitch, S., Smith, W. K., Wang, X., Zhu, Z., Haverd, V., Kato, E., Jain, A. K., Lienert, S., Lombardozzi, D., Nabel, J. E., Peylin, P., Poulter, B., and Zhu, D.: Contrasting effects of CO₂ fertilization, land-use change and warming on seasonal amplitude of Northern Hemisphere CO₂ exchange, *Atmospheric Chemistry and Physics*, 19, 12 361–12 375, <https://doi.org/10.5194/acp-19-12361-2019>, 2019.
- Battaglia, G. and Joos, F.: Marine N₂O Emissions From Nitrification and Denitrification Constrained by Modern Observations and Projected in Multimillennial Global Warming Simulations, *Global Biogeochemical Cycles*, 32, 92–121, <https://doi.org/10.1002/2017GB005671>, 2018.
- 620 Battipaglia, G., Saurer, M., Cherubini, P., Calfapietra, C., McCarthy, H. R., Norby, R. J., and Francesca Cotrufo, M.: Elevated CO₂ increases tree-level intrinsic water use efficiency: insights from carbon and oxygen isotope analyses in tree rings across three forest FACE sites, *New Phytologist*, 197, 544–554, <https://doi.org/10.1111/nph.12044>, 2013.
- Becker, M., Steinhoff, T., and Körtzinger, A.: A Detailed View on the Seasonality of Stable Carbon Isotopes Across the North Atlantic, *Global Biogeochemical Cycles*, 32, 1406–1419, <https://doi.org/10.1029/2018GB005905>, 2018.
- 625 Botía, S., Komiya, S., Marshall, J., Koch, T., Gałkowski, M., Lavric, J., Gomes-Alves, E., Walter, D., Fisch, G., Pinho, D. M., Nelson, B. W., Martins, G., Luijkx, I. T., Koren, G., Florentie, L., Carioca de Araújo, A., Sá, M., Andreae, M. O., Heimann, M., Peters, W., and Gerbig, C.: The CO₂ record at the Amazon Tall Tower Observatory: A new opportunity to study processes on seasonal and inter-annual scales, *Global Change Biology*, 28, 588–611, <https://doi.org/10.1111/gcb.15905>, 2022.
- Bugmann, H. and Christof, B.: Will the CO₂ fertilization effect in forests be offset by reduced tree longevity?, *Oecologia*, 165, 533–544, <https://doi.org/10.1007/s00442-010-1837-4>, 2011.
- 630



- Castro-Morales, K., Schürmann, G., Köstler, C., Rödenbeck, C., Heimann, M., and Zaehle, S.: Three decades of simulated global terrestrial carbon fluxes from a data assimilation system confronted with different periods of observations, *Biogeosciences*, 16, 3009–3032, <https://doi.org/10.5194/bg-16-3009-2019>, 2019.
- Cernusak, L. A. and Ubierna, N.: Carbon Isotope Effects in Relation to CO₂ Assimilation by Tree Canopies, pp. 291–310, Springer International Publishing, Cham, ISBN 978-3-030-92698-4, https://doi.org/10.1007/978-3-030-92698-4_9, 2022.
- 635 Cooperative Global Atmospheric Data Integration Project: Multi-laboratory compilation of synchronized and gap-filled atmospheric carbon dioxide records for the period 1979–2012 (obspack_co2_1_GLOBALVIEW-CO2_2013_v1.0.4_2013-12-23), <https://doi.org/10.3334/OBSPACK/1002>, 2013.
- Dargaville, R. J., Heimann, M., McGuire, A. D., Prentice, I. C., Kicklighter, D. W., Joos, F., Clein, J. S., Esser, G., Foley, J., Kaplan, J., Meier, R. A., Melillo, J. M., Moore, B., Ramankutty, N., Reichenau, T., Schloss, A., Sitch, S., Tian, H., Williams, L. J., and Wittenberg, U.: Evaluation of terrestrial carbon cycle models with atmospheric CO₂ measurements: Results from transient simulations considering increasing CO₂, climate, and land-use effects, *Global Biogeochemical Cycles*, 16, <https://doi.org/10.1029/2001gb001426>, 2002.
- 640 Farquhar, G.: Carbon Isotope Discrimination And Photosynthesis, *Annual Review of Plant Physiology and Plant Molecular Biology*, 40, 503–537, <https://doi.org/10.1146/annurev.arplant.40.1.503>, 1989.
- 645 Fay, A. R., Gregor, L., Landschützer, P., McKinley, G. A., Gruber, N., Gehlen, M., Iida, Y., Laruelle, G. G., Rödenbeck, C., Roobaert, A., and Zeng, J.: SeaFlux: harmonization of air–sea CO₂ fluxes from surface *p*CO₂ data products using a standardized approach, *Earth System Science Data*, 13, 4693–4710, <https://doi.org/10.5194/essd-13-4693-2021>, 2021.
- Forkel, M., Carvalhais, N., Rödenbeck, C., Keeling, R., Heimann, M., Thonicke, K., Zaehle, S., and Reichstein, M.: Enhanced seasonal CO₂ exchange caused by amplified plant productivity in northern ecosystems, *Science*, 351, 696–699, <https://doi.org/10.1126/science.aac4971>, 2016.
- 650 Francey, R. J., Tans, P. P., Allison, C. E., Enting, I. G., White, J. W. C., and Trolier, M.: Changes in oceanic and terrestrial carbon uptake since 1982, *Nature*, 373, 326–330, 1995.
- Frank, D. C., Poulter, B., Saurer, M., Esper, J., Huntingford, C., Helle, G., Treydte, K., Zimmermann, N. E., Schleser, G. H., Ahlstrom, A., Ciais, P., Friedlingstein, P., Levis, S., Lomas, M., Sitch, S., Viovy, N., Andreu-Hayles, L., Bednarz, Z., Berninger, F., Boettger, T., D’Alessandro, C. M., Daux, V., Filot, M., Grabner, M., Gutierrez, E., Haupt, M., Hilasvuori, E., Jungner, H., Kalela-Brundin, M., Krapiec, M., Leuenberger, M., Loader, N. J., Marah, H., Masson-Delmotte, V., Pazdur, A., Pawelczyk, S., Pierre, M., Planells, O., Pukiene, R., Reynolds-Henne, C. E., Rinne, K. T., Saracino, A., Sonninen, E., Stievenard, M., Switsur, V. R., Szczepanek, M., Szychowska-Krapiec, E., Todaro, L., Waterhouse, J. S., and Weigl, M.: Water-use efficiency and transpiration across European forests during the Anthropocene, *Nature Climate Change*, 5, 579–583, 2015.
- 660 Friedlingstein, P., O’Sullivan, M., Jones, M. W., Andrew, R. M., Hauck, J., Olsen, A., Peters, G. P., Peters, W., Pongratz, J., Sitch, S., Le Quéré, C., Canadell, J. G., Ciais, P., Jackson, R. B., Alin, S., Aragão, L. E., Arneeth, A., Arora, V., Bates, N. R., Becker, M., Benoit-Cattin, A., Bittig, H. C., Bopp, L., Bultan, S., Chandra, N., Chevallier, F., Chini, L. P., Evans, W., Florentie, L., Forster, P. M., Gasser, T., Gehlen, M., Gilfillan, D., Gkritzalis, T., Gregor, L., Gruber, N., Harris, I., Hartung, K., Haverd, V., Houghton, R. A., Ilyina, T., Jain, A. K., Joetzjer, E., Kadono, K., Kato, E., Kitidis, V., Korsbakken, J. I., Landschützer, P., Lefèvre, N., Lenton, A., Lienert, S., Liu, Z., Lombardozzi, D., Marland, G., Metzl, N., Munro, D. R., Nabel, J. E., Nakaoka, S. I., Niwa, Y., O’Brien, K., Ono, T., Palmer, P. I., Pierrot, D., Poulter, B., Resplandy, L., Robertson, E., Rödenbeck, C., Schwinger, J., Séférian, R., Skjelvan, I., Smith, A. J., Sutton, A. J., Tanhua, T., Tans, P. P., Tian, H., Tilbrook, B., Van Der Werf, G., Vuichard, N., Walker, A. P., Wanninkhof, R., Watson, A. J., Willis, D., Wiltshire, A. J., Yuan,



- W., Yue, X., and Zaehle, S.: Global Carbon Budget 2020, *Earth System Science Data*, 12, 3269–3340, <https://doi.org/10.5194/essd-12-3269-2020>, 2020.
- 670 GLOBALVIEW-CO2C13: Cooperative Atmospheric Data Integration Project - $\delta^{13}\text{C}$ of Carbon Dioxide, 2009.
- Gonsamo, A., D'Odorico, P., Chen, J. M., Wu, C., and Buchmann, N.: Changes in vegetation phenology are not reflected in atmospheric CO_2 and $^{13}\text{C}/^{12}\text{C}$ seasonality, *Global Change Biology*, 23, 4029–4044, <https://doi.org/10.1111/gcb.13646>, 2017.
- Graven, H. D., Keeling, R. F., Piper, S. C., Patra, P. K., Stephens, B. B., Wofsy, S. C., Welp, L. R., Sweeney, C., Tans, P. P., Kelley, J. J., Daube, B. C., Kort, E. A., Santoni, G. W., and Bent, J. D.: Enhanced Seasonal Exchange of CO_2 by Northern Ecosystems Since 1960, *Science*, 341, 1085–1089, <https://doi.org/10.1126/science.1239207>, 2013.
- 675 Gurney, K. R., Law, R. M., Denning, A. S., Rayner, P. J., Pak, B. C., Baker, D., Bousquet, P., Bruhwiler, L., Chen, Y.-H., Ciais, P., Fung, I. Y., Heimann, M., John, J., Maki, T., Maksyutov, S., Peylin, P., Prather, M., and Taguchi, S.: Transcom 3 inversion intercomparison: Model mean results for the estimation of seasonal carbon sources and sinks, *Global Biogeochemical Cycles*, 18, <https://doi.org/https://doi.org/10.1029/2003GB002111>, 2004.
- 680 Harris, I., Osborn, T. J., Jones, P., and Lister, D.: Version 4 of the CRU TS monthly high-resolution gridded multivariate climate dataset, *Scientific Data*, 7, 1–18, <https://doi.org/10.1038/s41597-020-0453-3>, 2020.
- Hauck, J. and Völker, C.: Rising atmospheric CO_2 leads to large impact of biology on Southern Ocean CO_2 uptake via changes of the Revelle factor, *Geophysical Research Letters*, 42, 1459–1464, <https://doi.org/10.1002/2015GL063070>, 2015.
- Heimann, M. and Körner, S.: The Global Atmospheric Tracer Model TM3, Tech. rep., Max-Planck-Institut für Biogeochemie, Max-Planck-Institut für Biogeochemie, Jena (Germany), 2003.
- 685 Heimann, M., Keeling, C. D., and Tucker, C. J.: A three dimensional model of atmospheric CO_2 transport based on observed winds: 3. Seasonal cycle and synoptic time scale variations, in: *Aspects of Climate Variability in the Pacific and the Western Americas*, pp. 277–303, American Geophysical Union (AGU), ISBN 9781118664285, <https://doi.org/10.1029/GM055p0277>, 1989.
- Heimann, M., Esser, G., Haxeltine, A., Kaduk, J., Kicklighter, D. W., Knorr, W., Kohlmaier, G. H., McGuire, A. D., Melillo, J., Moore, B., Otto, R. D., Prentice, I. C., Sauf, W., Schloss, A., Sitch, S., Wittenberg, U., and Würth, G.: Evaluation of terrestrial carbon cycle models through simulations of the seasonal cycle of atmospheric CO_2 : First results of a model intercomparison study, *Global Biogeochemical Cycles*, 12, 1–24, <https://doi.org/10.1029/97GB01936>, 1998.
- 690 Hurtt, G. C., Chini, L., Sahajpal, R., Frolking, S., Bodirsky, B. L., Calvin, K., Doelman, J. C., Fisk, J., Fujimori, S., Goldewijk, K. K., Hasegawa, T., Havlik, P., Heinemann, A., Humpenöder, F., Jungclaus, J., Kaplan, J. O., Kennedy, J., Krisztin, T., Lawrence, D., Lawrence, P., Ma, L., Mertz, O., Pongratz, J., Popp, A., Poulter, B., Riahi, K., Shevliakova, E., Stehfest, E., Thornton, P., Tubiello, F. N., van Vuuren, D. P., and Zhang, X.: Harmonization of global land use change and management for the period 850–2100 (LUH2) for CMIP6, *Geoscientific Model Development*, 13, 5425–5464, <https://doi.org/10.5194/gmd-13-5425-2020>, 2020.
- Ito, A., Inatomi, M., Huntzinger, D. N., Schwalm, C., Michalak, A. M., Cook, R., King, A. W., Mao, J., Wei, Y., Post, W. M., Wang, W., Arain, M. A., Huang, S., Hayes, D. J., Ricciuto, D. M., Shi, X., Huang, M., Lei, H., Tian, H., Lu, C., Yang, J., Tao, B., Jain, A., Poulter, B., Peng, S., Ciais, P., Fisher, J. B., Parazoo, N., Schaefer, K., Peng, C., Zeng, N., and Zhao, F.: Decadal trends in the seasonal-cycle amplitude of terrestrial CO_2 exchange resulting from the ensemble of terrestrial biosphere models, *Tellus B: Chemical and Physical Meteorology*, 68, 28 968, <https://doi.org/10.3402/tellusb.v68.28968>, 2016.
- 700 Jeltsch-Thömmes, A. and Joos, F.: Modeling the evolution of pulse-like perturbations in atmospheric carbon and carbon isotopes: The role of weathering-sedimentation imbalances, *Climate of the Past*, 16, 423–451, <https://doi.org/10.5194/cp-16-423-2020>, 2020.



- 705 Jeltsch-Thömmes, A. and Joos, F.: Carbon cycle responses to changes in weathering and the long-term fate of stable carbon isotopes, *Paleoceanography and Paleoclimatology*, p. accepted, 2023.
- Jin, Y., Keeling, R. F., Stephens, B. B., Long, M. C., Patra, P. K., Rödenbeck, C., Morgan, E. J., Kort, E. A., and Sweeney, C.: Improved atmospheric constraints on Southern Ocean CO₂ exchange, *Proceedings of the National Academy of Sciences*, 121, e2309333 121, <https://doi.org/10.1073/pnas.2309333121>, 2024.
- 710 Joos, F. and Bruno, M.: Long-term variability of the terrestrial and oceanic carbon sinks and the budgets of the carbon isotopes ¹³C and ¹⁴C, *Global Biogeochemical Cycles*, 12, 277–295, <https://doi.org/10.1029/98GB00746>, 1998.
- Joos, F., Hameau, A., Frölicher, T. L., and Stephenson, D. B.: Anthropogenic Attribution of the Increasing Seasonal Amplitude in Surface Ocean pCO₂, *Geophysical Research Letters*, 50, e2023GL102857, <https://doi.org/10.1029/2023GL102857>, e2023GL102857 2023GL102857, 2023.
- 715 Kalnay, E., Kanamitsu, M., Kistler, R., Collins, W., Deaven, D., Gandin, L., Iredell, M., Saha, S., White, G., Woollen, J., Zhu, Y., Leetmaa, A., Reynolds, R., Chelliah, M., Ebisuzaki, W., Higgins, W., Janowiak, J., Mo, K. C., Ropelewski, C., Wang, J., Jenne, R., and Joseph, D.: The NCEP/NCAR 40-Year Reanalysis Project, *Bulletin of the American Meteorological Society*, 77, 437–471, [https://doi.org/10.1175/1520-0477\(1996\)077<0437:TNYRP>2.0.CO;2](https://doi.org/10.1175/1520-0477(1996)077<0437:TNYRP>2.0.CO;2), 1996.
- Kaminski, T., Heimann, M., and Giering, R.: A Global Scale Inversion of the Transport of CO₂ Based on a Matrix Representation of an Atmospheric Transport Model Derived by Its Adjoint, in: *Air Pollution Modeling and Its Application XII*, pp. 247–255, Springer US, Boston, MA, https://doi.org/10.1007/978-1-4757-9128-0_26, 1998.
- 720 Kauwe, M. G., Medlyn, B. E., Zaehle, S., Walker, A. P., Dietze, M. C., Hickler, T., Jain, A. K., Luo, Y., Parton, W. J., Prentice, I. C., Smith, B., Thornton, P. E., Wang, S., Wang, Y.-P., Wårlind, D., Weng, E., Crous, K. Y., Ellsworth, D. S., Hanson, P. J., Kim, H.-S., Warren, J. M., Oren, R., and Norby, R. J.: Forest water use and water use efficiency at elevated CO₂: a model-data intercomparison at two contrasting temperate forest FACE sites, *Global Change Biology*, 19, 1759–1779, <https://doi.org/10.1111/gcb.12164>, 2013.
- Keeling, C. D.: The Concentration and Isotopic Abundances of Carbon Dioxide in the Atmosphere, *Tellus*, 12, 200–203, <https://doi.org/10.1111/j.2153-3490.1960.tb01300.x>, 1960.
- Keeling, C. D., Carter, A. F., and Mook, W. G.: Seasonal, latitudinal, and secular variations in the abundance and isotopic ratios of atmospheric CO₂: 2. Results from oceanographic cruises in the tropical Pacific Ocean, *Journal of Geophysical Research: Atmospheres*, 89, 4615–4628, <https://doi.org/10.1029/JD089iD03p04615>, 1984.
- 730 Keeling, C. D., Bollen, B. R., Fung, C. A., Piper, S. C., Whorf, T. P., Heimann, M., Mook, W. G., and Roeloffzen, H.: A three dimensional model of atmospheric CO₂ transport based on observed winds: 1. Analysis of Observational Data, in: *Aspects of Climate Variability in the Pacific and the Western Americas*, pp. 165–236, American Geophysical Union (AGU), ISBN 9781118664285, <https://doi.org/10.1029/GM055p0277>, 1989.
- 735 Keeling, C. D., Chin, J. F. S., and Whorf, T. P.: Increased activity of northern vegetation inferred from atmospheric CO₂ measurements, *Nature*, 382, 146–149, <https://doi.org/10.1038/382146a0>, 1996.
- Keeling, C. D., Piper, S. C., Bacastow, R. B., Wahlen, M., Whorf, T. P., Heimann, M., and Meijer, H. A.: Exchanges of atmospheric CO₂ and ¹³CO₂ with the terrestrial biosphere and oceans from 1978 to 2000. I. Global aspects, *SIO Reference Series*, No. 01-06, Scripps Institution of Oceanography, San Diego, p. 88, 2001.
- 740 Keeling, C. D., Piper, S. C., Bacastow, R. B., Wahlen, M., Whorf, T. P., Heimann, M., and Meijer, H. A.: Atmospheric CO₂ and ¹³CO₂ Exchange with the Terrestrial Biosphere and Oceans from 1978 to 2000: Observations and Carbon Cycle Implications, in: *A History of Atmospheric CO₂ and Its Effects on Plants, Animals, and Ecosystems*, edited by Baldwin, I. T., Caldwell, M. M., Heldmaier, G., Jackson,



- R. B., Lange, O. L., Mooney, H. A., Schulze, E.-D., Sommer, U., Ehleringer, J. R., Denise Dearing, M., and Cerling, T. E., pp. 83–113, Springer New York, New York, NY, ISBN 978-0-387-27048-7, https://doi.org/10.1007/0-387-27048-5_5, 2005.
- 745 Keenan, T. F., Hollinger, D. Y., Bohrer, G., Dragoni, D., Munger, J. W., Schmid, H. P., and Richardson, A. D.: Increase in forest water-use efficiency as atmospheric carbon dioxide concentrations rise, *Nature*, 499, 324–327, <https://doi.org/10.1038/nature12291>, 2013.
- Keller, K. M., Joos, F., and Raible, C. C.: Time of emergence of trends in ocean biogeochemistry, *Biogeosciences*, 11, 3647–3659, <https://doi.org/10.5194/bg-11-3647-2014>, 2014.
- Keller, K. M., Lienert, S., Bozbiyik, A., Stocker, T. F., Churakova (Sidorova), O. V., Frank, D. C., Klesse, S., Koven, C. D., Leuenberger, M.,
750 Riley, W. J., Saurer, M., Siegwolf, R., Weigt, R. B., and Joos, F.: 20th century changes in carbon isotopes and water-use efficiency: tree-ring-based evaluation of the CLM4.5 and LPX-Bern models, *Biogeosciences*, 14, 2641–2673, <https://doi.org/10.5194/bg-14-2641-2017>, 2017.
- Knauer, J., Zaehle, S., Reichstein, M., Medlyn, B. E., Forkel, M., Hagemann, S., and Werner, C.: The response of ecosystem water-use efficiency to rising atmospheric CO₂ concentrations: sensitivity and large-scale biogeochemical implications, *New Phytologist*, 213, 1654–
755 1666, <https://doi.org/10.1111/nph.14288>, 2017.
- Körner, C.: A matter of tree longevity, *Science*, 355, 130–131, <https://doi.org/10.1126/science.aal2449>, 2017.
- Landschützer, P., Gruber, N., Bakker, D. C. E., and Schuster, U.: Recent variability of the global ocean carbon sink, *Global Biogeochemical Cycles*, 28, 927–949, <https://doi.org/10.1002/2014GB004853>, 2014.
- Lienert, S. and Joos, F.: A Bayesian ensemble data assimilation to constrain model parameters and land-use carbon emissions, *Biogeosciences*, 15, 2909–2930, <https://doi.org/10.5194/bg-15-2909-2018>, 2018.
- 760 Lloyd, J. and Farquhar, G.: C₁₃ discrimination during CO₂ assimilation by the terrestrial biosphere, *Oecologia*, 99, 201–215, <https://doi.org/10.1007/BF00627732>, 1994.
- Long, M. C., Stephens, B. B., McKain, K., Sweeney, C., Keeling, R. F., Kort, E. A., Morgan, E. J., Bent, J. D., Chandra, N., Chevallier, F., Commane, R., Daube, B. C., Krümmel, P. B., Loh, Z., Luijkx, I. T., Munro, D., Patra, P., Peters, W., Ramonet, M., Rödenbeck, C.,
765 Stavert, A., Tans, P., and Wofsy, S. C.: Strong Southern Ocean carbon uptake evident in airborne observations, *Science*, 374, 1275–1280, <https://doi.org/10.1126/science.abi4355>, 2021.
- Majkut, J. D., Carter, B. R., Frölicher, T. L., Dufour, C. O., Rodgers, K. B., and Sarmiento, J. L.: An observing system simulation for Southern Ocean carbon dioxide uptake, *Philosophical Transactions of the Royal Society A: Mathematical, Physical and Engineering Sciences*, 372, 20130 046, <https://doi.org/10.1098/rsta.2013.0046>, 2014.
- 770 Masarie, K. A., Peters, W., Jacobson, A. R., and Tans, P. P.: ObsPack: a framework for the preparation, delivery, and attribution of atmospheric greenhouse gas measurements, *Earth System Science Data*, 6, 375–384, <https://doi.org/10.5194/essd-6-375-2014>, 2014.
- Menviel, L., Mouchet, A., Meissner, K. J., Joos, F., and England, M. H.: Impact of oceanic circulation changes on atmospheric $\delta^{13}\text{C}_{\text{CO}_2}$, *Global Biogeochemical Cycles*, 29, 1944–1961, <https://doi.org/10.1002/2015GB005207>, 2015.
- Mook, W.: ¹³C in atmospheric CO₂, *Netherlands Journal of Sea Research*, 20, 211–223, [https://doi.org/10.1016/0077-7579\(86\)90043-8](https://doi.org/10.1016/0077-7579(86)90043-8),
775 1986.
- Peng, S., Ciais, P., Chevallier, F., Peylin, P., Cadule, P., Sitch, S., Piao, S., Ahlström, A., Huntingford, C., Levy, P., Li, X., Liu, Y., Lomas, M., Poulter, B., Viovy, N., Wang, T., Wang, X., Zaehle, S., Zeng, N., Zhao, F., and Zhao, H.: Benchmarking the seasonal cycle of CO₂ fluxes simulated by terrestrial ecosystem models, *Global Biogeochemical Cycles*, 29, 46–64, <https://doi.org/10.1002/2014GB004931>, 2015.



- Peylin, P., Law, R. M., Gurney, K. R., Chevallier, F., Jacobson, A. R., Maki, T., Niwa, Y., Patra, P. K., Peters, W., Rayner, P. J., Rödenbeck, C.,
780 Van Der Laan-Luijkx, I. T., and Zhang, X.: Global atmospheric carbon budget: Results from an ensemble of atmospheric CO₂ inversions,
Biogeosciences, 10, 6699–6720, <https://doi.org/10.5194/bg-10-6699-2013>, 2013.
- Peylin, P., Bacour, C., MacBean, N., Leonard, S., Rayner, P., Kuppel, S., Koffi, E., Kane, A., Maignan, F., Chevallier, F., Ciais, P., and Prunet,
P.: A new stepwise carbon cycle data assimilation system using multiple data streams to constrain the simulated land surface carbon cycle,
Geoscientific Model Development, 9, 3321–3346, <https://doi.org/10.5194/gmd-9-3321-2016>, 2016.
- 785 Peñuelas, J., Canadell, J. G., and Ogaya, R.: Increased water-use efficiency during the 20th century did not translate into enhanced tree
growth, Global Ecology and Biogeography, 20, 597–608, <https://doi.org/10.1111/j.1466-8238.2010.00608.x>, 2011.
- Piao, S., Liu, Z., Wang, Y., Ciais, P., Yao, Y., Peng, S., Chevallier, F., Friedlingstein, P., Janssens, I. A., Peñuelas, J., Sitch, S.,
and Wang, T.: On the causes of trends in the seasonal amplitude of atmospheric CO₂, Global Change Biology, 24, 608–616,
<https://doi.org/10.1111/gcb.13909>, 2018.
- 790 Quay, P. D., Sonnerup, R., Munro, D. R., and Sweeney, C.: Anthropogenic CO₂ accumulation and uptake rates in the Pa-
cific Ocean based on changes in the 13 C/ 12 C of dissolved inorganic carbon, Global Biogeochemical Cycles, 31, 59–80,
<https://doi.org/10.1002/2016GB005460>, 2017.
- Ritz, S. P., Stocker, T. F., Joos, F., Ritz, S. P., Stocker, T. F., and Joos, F.: A Coupled Dynamical Ocean–Energy Balance Atmosphere Model
for Paleoclimate Studies, Journal of Climate, 24, 349–375, <https://doi.org/10.1175/2010JCLI3351.1>, 2011.
- 795 Saurer, M. and Voelker, S.: Intrinsic Water-Use Efficiency Derived from Stable Carbon Isotopes of Tree-Rings, pp. 481–498, Springer
International Publishing, Cham, ISBN 978-3-030-92698-4, https://doi.org/10.1007/978-3-030-92698-4_17, 2022.
- Saurer, M., Spahni, R., Frank, D. C., Joos, F., Leuenberger, M., Loader, N. J., McCarroll, D., Gagen, M., Poulter, B., Siegwolf, R. T., Andreu-
Hayles, L., Boettger, T., Dorado Liñán, I., Fairchild, I. J., Friedrich, M., Gutierrez, E., Haupt, M., Hilasvuori, E., Heinrich, I., Helle, G.,
Grudd, H., Jalkanen, R., Levanič, T., Linderholm, H. W., Robertson, I., Sonninen, E., Treydte, K., Waterhouse, J. S., Woodley, E. J., Wynn,
800 P. M., and Young, G. H.: Spatial variability and temporal trends in water-use efficiency of European forests, Global Change Biology, 20,
3700–3712, <https://doi.org/10.1111/gcb.12717>, 2014.
- Scholze, M., Kaplan, J. O., Knorr, W., and Heimann, M.: Climate and interannual variability of the atmosphere-biosphere 13CO₂ flux,
Geophysical Research Letters, 30, 1–4, <https://doi.org/10.1029/2002GL015631>, 2003.
- Scholze, M., Ciais, P., and Heimann, M.: Modeling terrestrial 13C cycling: Climate, land use and fire, Global Biogeochemical Cycles, 22,
805 1–13, <https://doi.org/10.1029/2006GB002899>, 2008.
- Schürmann, G. J., Kaminski, T., Köstler, C., Carvalhais, N., Voßbeck, M., Kattge, J., Giering, R., Rödenbeck, C., Heimann, M., and Zaehle,
S.: Constraining a land-surface model with multiple observations by application of the MPI-Carbon Cycle Data Assimilation System V1.0,
Geoscientific Model Development, 9, 2999–3026, <https://doi.org/10.5194/gmd-9-2999-2016>, 2016.
- Sitch, S., Smith, B., Prentice, I. C., Arneth, A., Bondeau, A., Cramer, W., Kaplan, J. O., Levis, S., Lucht, W., Sykes, M. T., Thonicke, K.,
810 and Venevsky, S.: Evaluation of ecosystem dynamics, plant geography and terrestrial carbon cycling in the LPJ dynamic global vegetation
model, Global Change Biology, 9, 161–185, <https://doi.org/10.1046/j.1365-2486.2003.00569.x>, 2003.
- Still, C. J., Berry, J. A., Collatz, G. J., and DeFries, R. S.: Global distribution of C₃ and C₄ vegetation: Carbon cycle implications, Global
Biogeochemical Cycles, 17, 6–16–14, <https://doi.org/10.1029/2001GB001807>, 2003.
- Stocker, B. D., Spahni, R., and Joos, F.: DYPTOP: a cost-efficient TOPMODEL implementation to simulate sub-grid spatio-temporal dy-
815 namics of global wetlands and peatlands, Geoscientific Model Development, 7, 3089–3110, <https://doi.org/10.5194/gmd-7-3089-2014>,
2014.



- Strassmann, K. M., Joos, F., and Fischer, G.: Simulating effects of land use changes on carbon fluxes: past contributions to atmospheric CO₂ increases and future commitments due to losses of terrestrial sink capacity, *Tellus B*, 60, 583–603, 2008.
- 820 Takahashi, T., Sutherland, S. C., Wanninkhof, R., Sweeney, C., Feely, R. A., Chipman, D. W., Hales, B., Friederich, G., Chavez, F., Sabine, C., Watson, A., Bakker, D. C., Schuster, U., Metzl, N., Yoshikawa-Inoue, H., Ishii, M., Midorikawa, T., Nojiri, Y., Körtzinger, A., Steinhoff, T., Hoppema, M., Olafsson, J., Arnarson, T. S., Tilbrook, B., Johannessen, T., Olsen, A., Bellerby, R., Wong, C., Delille, B., Bates, N., and de Baar, H. J.: Climatological mean and decadal change in surface ocean pCO₂, and net sea–air CO₂ flux over the global oceans, *Deep Sea Research Part II: Topical Studies in Oceanography*, 56, 554–577, <https://doi.org/10.1016/j.dsr2.2008.12.009>, 2009.
- Tans, P. P., Berry, J. A., and Keeling, R. F.: Oceanic 13C/12C observations: A new window on ocean CO₂ uptake, *Global Biogeochemical Cycles*, 7, 353–368, <https://doi.org/https://doi.org/10.1029/93GB00053>, 1993.
- 825 Tian, H., Yang, J., Lu, C., Xu, R., Canadell, J. G., Jackson, R. B., Arneeth, A., Chang, J., Chen, G., Ciais, P., Gerber, S., Ito, A., Huang, Y., Joos, F., Lienert, S., Messina, P., Olin, S., Pan, S., Peng, C., Saikawa, E., Thompson, R. L., Vuichard, N., Winiwarer, W., Zaehle, S., Zhang, B., Zhang, K., and Zhu, Q.: The Global N₂O Model Intercomparison Project, *Bulletin of the American Meteorological Society*, 99, 1231–1251, <https://doi.org/10.1175/BAMS-D-17-0212.1>, 2018.
- 830 Trudinger, C. M., Enting, I. G., Rayner, P. J., and Francey, R. J.: Kalman filter analysis of ice core data 2. Double deconvolution of CO₂ and δ¹³C measurements, *Journal of Geophysical Research: Atmospheres*, 107, ACH 5–1–ACH 5–24, <https://doi.org/https://doi.org/10.1029/2001JD001112>, 2002.
- van der Velde, I. R., Miller, J. B., Schaefer, K., Masarie, K. A., Denning, S., White, J. W. C., Tans, P. P., Krol, M. C., and Peters, W.: Biosphere model simulations of interannual variability in terrestrial 13C/12C exchange, *Global Biogeochemical Cycles*, 27, 637–649, <https://doi.org/https://doi.org/10.1002/gbc.20048>, 2013.
- 835 Voelker, S. L., Brooks, J. R., Meinzer, F. C., Anderson, R., Bader, M. K.-F., Battipaglia, G., Becklin, K. M., Beerling, D., Bert, D., Betancourt, J. L., Dawson, T. E., Domec, J.-C., Guyette, R. P., Körner, C., Leavitt, S. W., Linder, S., Marshall, J. D., Mildner, M., Ogée, J., Panyushkina, I., Plumpton, H. J., Pregitzer, K. S., Saurer, M., Smith, A. R., Siegwolf, R. T. W., Stambaugh, M. C., Talhelm, A. F., Tardif, J. C., Van de Water, P. K., Ward, J. K., and Wingate, L.: A dynamic leaf gas-exchange strategy is conserved in woody plants under changing ambient CO₂: evidence from carbon isotope discrimination in paleo and CO₂ enrichment studies, *Global Change Biology*, 22, 889–902, <https://doi.org/10.1111/gcb.13102>, 2016.
- 840 Walker, A. P., De Kauwe, M. G., Bastos, A., Belmecheri, S., Georgiou, K., Keeling, R. F., McMahon, S. M., Medlyn, B. E., Moore, D. J., Norby, R. J., Zaehle, S., Anderson-Teixeira, K. J., Battipaglia, G., Brienen, R. J., Cabugao, K. G., Cailleret, M., Campbell, E., Canadell, J. G., Ciais, P., Craig, M. E., Ellsworth, D. S., Farquhar, G. D., Fatichi, S., Fisher, J. B., Frank, D. C., Graven, H., Gu, L., Haverd, V., Heilman, K., Heimann, M., Hungate, B. A., Iversen, C. M., Joos, F., Jiang, M., Keenan, T. F., Knauer, J., Körner, C., Leshyk, V. O., Leuzinger, S., Liu, Y., MacBean, N., Malhi, Y., McVicar, T. R., Penuelas, J., Pongratz, J., Powell, A. S., Riutta, T., Sabot, M. E., Schleucher, J., Sitch, S., Smith, W. K., Sulman, B., Taylor, B., Terrer, C., Torn, M. S., Treseder, K. K., Trugman, A. T., Trumbore, S. E., van Mantgem, P. J., Voelker, S. L., Whelan, M. E., and Zuidema, P. A.: Integrating the evidence for a terrestrial carbon sink caused by increasing atmospheric CO₂, *New Phytologist*, 229, 2413–2445, <https://doi.org/10.1111/nph.16866>, 2021.
- 845 Wang, S., Zhang, Y., Ju, W., Chen, J. M., Ciais, P., Cescatti, A., Sardans, J., Janssens, I. A., Wu, M., Berry, J. A., Campbell, E., Fernández-Martínez, M., Alkama, R., Sitch, S., Friedlingstein, P., Smith, W. K., Yuan, W., He, W., Lombardozzi, D., Kautz, M., Zhu, D., Lienert, S., Kato, E., Poulter, B., Sanders, T. G. M., Krüger, I., Wang, R., Zeng, N., Tian, H., Vuichard, N., Jain, A. K., Wiltshire, A., Haverd, V., Goll, D. S., and Peñuelas, J.: Recent global decline of CO₂ fertilization effects on vegetation photosynthesis, *Science*, 370, 1295–1300, <https://doi.org/10.1126/science.abb7772>, 2020.



- 855 Wania, R., Ross, I., and Prentice, I. C.: Integrating peatlands and permafrost into a dynamic global vegetation model: 1. Evaluation and sensitivity of physical land surface processes, *Global Biogeochemical Cycles*, 23, 1–19, <https://doi.org/10.1029/2008GB003412>, 2009a.
- Wania, R., Ross, I., and Prentice, I. C.: Integrating peatlands and permafrost into a dynamic global vegetation model: 2. Evaluation and sensitivity of vegetation and carbon cycle processes, *Global Biogeochemical Cycles*, 23, 1–15, <https://doi.org/10.1029/2008GB003413>, 2009b.
- 860 Welch, B. L.: The Generalization of ‘Student’s’ Problem when Several Different Population Variances are Involved, *Biometrika*, 34, 28–35, <https://doi.org/10.2307/2332510>, 1947.
- Xu-Ri and Prentice, I. C.: Terrestrial nitrogen cycle simulation with a dynamic global vegetation model, *Global Change Biology*, 14, 1745–1764, <https://doi.org/10.1111/j.1365-2486.2008.01625.x>, 2008.